

Spectral library of age-benchmark low-mass stars and brown dwarfs ^{*}

E. Manjavacas^{1,2} †, N. Lodieu^{3,4}, V. J. S. Béjar^{3,4}, M. R. Zapatero-Osorio⁵, S. Boudreault⁶, M. Bonnefoy⁷

¹ *W. M. Keck Observatory, 65-1120 Mamalahoa Highway, Kamuela, HI 96743, USA.*

² *Department of Astronomy/Steward Observatory, The University of Arizona, 933 N. Cherry Avenue, Tucson, AZ, 85721, USA.*

³ *Instituto de Astrofísica de Canarias, C/ Vía Láctea, s/n, E38205, La Laguna (Tenerife), Spain.*

⁴ *Dpt. de Astrofísica, Univ. de La Laguna, Avda. Astrofísico Francisco Sánchez s/n, 38206, La Laguna (Tenerife), Spain.*

⁵ *Centro de Astrobiología (CSIC-INTA), Crta. Ajalvir km 4, E-28850 Torrejón de Ardoz, Madrid, Spain.*

⁶ *Max-Planck-Institut für Sonnensystemforschung, Justus-von-Liebig-Weg 3, 37077, Göttingen, Germany.*

⁷ *Université Grenoble Alpes, CNRS, IPAG, 38000 Grenoble, France.*

2 February 2022

ABSTRACT

In the past years, some extremely red brown dwarfs were found. They were believed to have low surface gravity, but many of their spectral characteristics were similar to those of high surface gravity brown dwarfs, showing that youth spectral characteristics are poorly understood. We aim to test surface gravity indicators in late-M and early-L brown dwarf spectra using data obtained with the X-shooter spectrograph at the Very Large Telescope. We selected a benchmark sample of brown dwarfs members of Chamaeleon I (~ 2 Myr), Upper Scorpius (5–10 Myr), Pleiades (132 ± 27 Myr), and Praesepe (590–790 Myr) with well-constrained ages, and similar metallicities. We provided a consistent spectral classification of the sample in the optical and in the near-infrared. We measured the equivalent widths of their alkali lines, finding that they have a moderate correlation with age, especially for objects with spectral types M8 and later. We used spectral indices defined in the literature to estimate surface gravity, finding that their gravity assignment is accurate for 75% of our sample. We investigated the correlation between red colours and age, finding that after ~ 10 Myr, the colour does not change significantly for our sample with spectral types M6.0–L3.0. In this case, red colours might be associated with circumstellar disks, ring structures, extinction, or viewing angle. Finally, we calculated the bolometric luminosity, and J and K bolometric corrections for our sample. We found that six objects are overluminous compared to other members of the same association. Those objects are also flagged as binary candidates by the *Gaia* survey.

Key words: stars: brown dwarfs, fundamental parameters

1 INTRODUCTION

Brown dwarfs are substellar objects that are unable to sustain hydrogen fusion. Since they are born, brown dwarfs cool down with time and contract. During this process, brown dwarfs change spectral types, through the M, L, T and Y, changing their luminosity and chemistry (Kirkpatrick et al. 2012). Due to this evolution, spectral types do not constrain substellar masses, and we additionally need ages to esti-

mate masses using evolutionary models for substellar objects (Burrows et al. 1997; Baraffe et al. 2015).

Brown dwarfs contract as they cool down over their lifetime, therefore, younger brown dwarfs (< 100 Myr) have larger radii and lower gravity ($g = GM/R^2$) than their older counterpart in the field (> 500 Myr). Young brown dwarfs and exoplanet atmospheres are expected to share similar colours, temperatures and surface gravities (Chauvin et al. 2004; Marois et al. 2008; Faherty et al. 2013). Nevertheless, isolated young brown dwarfs, unlike exoplanets, are isolated and not close to their parent star, which make them easier to observe, especially for spectroscopic studies. The study of young free-floating brown dwarf are excellent proxies to

^{*} Based on observations of VLT/XSHOOTER, under the program ID 098.C-0277.

† E-mail: emanjavacas@keck.hawaii.edu

improve our view of the atmospheres of imaged young giant exoplanets.

Gravity affects brown dwarf atmospheres, changing their spectral characteristics. Many atomic lines and molecular bands are weaker in spectra of young brown dwarfs than for their higher gravity counterparts. The neutral alkali lines are weaker over the whole optical and near-infrared spectrum: Rb I at 794.8 nm, Na I at 818.3 nm, Na I at 819.5 nm, Cs I at 852.0 nm, KI at 1169 nm, KI at 1177 nm, KI at 1243 nm and KI at 1253 nm (Martín et al. 1996; Gorlova et al. 2003; McGovern et al. 2004; Martín et al. 2017, and references therein. See Schlieder et al. 2012, for a theoretical explanation). In addition, FeH absorptions in the *J* and *H*-bands are also less prominent for low gravity dwarfs (Allers & Liu 2013; Lodieu et al. 2018, among others). In contrast, the VO bands at 0.74, 0.96, 1.06 μm and 1.18 μm , and the TiO bands at 0.71, 0.76, 0.82, 0.84, and 1.25 μm are stronger for low-surface gravity objects (Martín et al. 1996; Zapatero Osorio et al. 1997; Allers & Liu 2013, and references therein), particularly in L-dwarfs (Allers & Liu 2013), due to inefficient condensation (Lodders 2002). In addition, very red colours were also believed to be an indication of low surface gravity, as it was expected to prevent the dust settlement of the upper atmosphere. In the past years, several tens of very red L brown dwarfs (Kirkpatrick et al. 2006; Stephens et al. 2009; Gizis et al. 2012; Liu et al. 2013; Marocco et al. 2014; Filippazzo et al. 2015; Faherty et al. 2016; Liu et al. 2016; Schneider et al. 2014, 2017; Best et al. 2017, among others) have been found in large surveys, like 2MASS (The Two Micron All Sky Survey, Skrutskie et al. 2006), SDSS (Sloan Digital Sky Survey, Blanton et al. 2017), and PanStarrs (Panoramic Survey Telescope and Rapid Response System, Chambers et al. 2016). These very red brown dwarfs were believed to be young, nonetheless, some objects did not exhibit clear spectroscopic signposts of low gravity atmospheres in their spectra, like for example, weak alkali lines. This is the case of ULAS J222711-004547 (Marocco et al. 2014), 2MASS J035523.37+113343.7 (Faherty et al. 2013), and WISEP J004701.06+680352.1 (Gizis et al. 2015), among others. These examples suggest that red colours *alone* cannot be used as a youth signature.

In this paper, we aim to test the most common methods to estimate surface gravity (i.e. age) in brown dwarfs. To achieve this aim, we targeted spectra of members of open clusters and associations with well-determined ages. We selected 20 members to the Chamaeleon I (Cha I) region (~ 2 Myr, Luhman 2007), the Upper Scorpius (UppSco) association (5–10 Myr, Slesnick et al. 2008; Song et al. 2012; Feiden 2016; Pecaut & Mamajek 2016; Rizzuto et al. 2016; Fang et al. 2017), the Pleiades open cluster (132 ± 27 Myr, Stauffer et al. 1998; Barrado y Navascués 2004; Dahm 2015; Lodieu et al. 2019), and the Praesepe open cluster (590–790 Myr, Fossati et al. 2008; Delorme et al. 2011; Brandt & Huang 2015; Gossage et al. 2018). The ages of these associations or open clusters correspond respectively to the gravities that defined the γ , β and α for low, intermediate and field gravity classification of M and L dwarfs (Cruz et al. 2009), or the VL-G (Very Low Gravity), INT-G (Intermediate Gravity) and FLD-G (Field Gravity) classes defined by Allers & Liu (2013).

In Section 2, we describe the selected sample of objects presented in this paper. In Section 3, we provide details on

the X-shooter observations and data reduction. In Section 4 we explain the analysis carried out and our results. In Section 5 we derived physical parameters for our sample using evolutionary models for substellar objects. Finally, in Section 6 we summarise our results.

Table 1. List of observed targets with their full names, coordinates, magnitudes, spectral types, cluster or association memberships, and flags for disk bearing sources and binary candidates.

Num.	Name	RA	DEC	J [mag]	Opt SpT	NIR SpT	Open Cluster/Association	Disk	Binary candidate?	Ref.
1	UGCS J083748.00+201448.5	08 37 48.01	+20 14 48.6	16.50±0.01			Praesepe (590–790 Myr)	NR ^a	NR ^b	1
2	2MASS J08370215+1952074	08 37 02.13	+19 52 07.4	15.69±0.01	M7 [29]		Praesepe (590–790 Myr)	NR ^a	Yes	2, 31
3	UGCS J083654.60+195415.7	08 36 54.60	+19 54 15.7	17.11±0.02			Praesepe (590–790 Myr)	NR ^a	NR ^b	2
4	2MASS J08410852+1954018	08 41 08.54	+19 54 01.0	16.45±0.01			Praesepe (590–790 Myr)	NR ^a	Yes	2, 31
5	2MASS J08370450+2016033	08 37 04.49	+20 16 03.2	16.82±0.02			Praesepe (590–790 Myr)	NR ^a	Yes	3, 31
6	UGCS J084510.65+214817.0	08 45 10.66	+21 48 17.1	17.42±0.03	L0.5 [28]		Praesepe (590–790 Myr)	NR ^a	Yes	3, 31
7	2MASS J03484469+2437236	03 48 44.69	+24 37 23.6	14.90±0.01		M5.5 [25]	Pleiades (132±27 Myr)	NR ^a	Yes	4, 31
8	2MASS J03491512+2436225	03 49 15.12	+24 36 22.5	15.17±0.01	M6.5 [27]	M6.5 [25]	Pleiades (132±27 Myr)	NR ^a	NR ^b	5
9	2MASS J03512557+2345214	03 51 25.57	+23 45 21.4	16.13±0.03	M8.0 [26]	M8.0 [25]	Pleiades (132±27 Myr)	NR ^a	NR ^b	6
10	2MASS J03443516+2513429	03 44 35.16	+25 13 42.9	15.66±0.01		M9.3 [25]	Pleiades (132±27 Myr)	NR ^a	Yes	7, 31
11	2MASS J03463425+2350036	03 46 34.25	+23 50 03.6	17.46±0.03			Pleiades (132±27 Myr)	NR ^a	NR ^b	8
12	2MASS J03461406+2321565	03 46 14.06	+23 21 56.5	15.67±0.02			Pleiades (132±27 Myr)	NR ^a	NR ^b	9
13	2MASS J03541027+2341402	03 54 10.27	+23 41 40.2	18.14±0.05		L3.0 [25]	Pleiades (132±27 Myr)	NR ^a	NR ^b	10
14	2MASS J15591135-2338002	15 59 11.35	-23 38 00.2	14.40±0.04	M7.0 [11]		UppSco (5–10 Myr)	Yes	NR ^b	11, 17
15	2MASS J16060391-2056443	16 06 03.91	-20 56 44.3	13.53±0.03	M7.0 [24]		UppSco (5–10 Myr)	Yes	NR ^b	12, 18
16	2MASS J16060629-2335133	16 06 06.29	-23 35 13.3	16.23±0.01	M9 [23]	L0.0 [13]	UppSco (5–10 Myr)	NR ^a	NR ^b	13
17	2MASS J11085497-7632410	11 08 54.97	-76 32 41.0	13.06±0.03	M5.5 [22]		Cha I (~2 Myr)	Yes	NR ^b	14, 19
18	2MASS J11123099-7653342	11 12 30.99	-76 53 34.2	14.07±0.03	M7.0 [21]	M7.0 [21]	Cha I (~2 Myr)	NR ^a	NR ^b	15
19	2MASS J11074656-7615174	11 07 46.56	-76 15 17.4	13.94±0.03	M6.5 [30]		Cha I (~2 Myr)	Yes	NR ^b	30
20	2MASS J11062554-7633418	11 06 25.54	-76 33 41.8	13.00±0.03	M5.5 [30]		Cha I (~2 Myr)	Yes	NR ^b	30

References: [1] - Boudreault et al. (2010), [2] - Hodgkin et al. (1999), [3] - Boudreault et al. (2012), [4] - Bouvier et al. (1998), [5] - Stauffer et al. (1998), [6] - Bouvier et al. (1998), [7] - Bouvier et al. (1998), [8] - Nagashima et al. (2003), [9] - Lodieu et al. (2012a), [10] - Bihain et al. (2006), [11] - Ardila et al. (2000), [12] - Martín et al. (2004), [13] - Lodieu et al. (2007), [14] - Persi et al. (2000), [15] - López Martí et al. (2004).

References of disks detections: [16] - Luhman & Muench (2008), [17] - van der Plas et al. (2016), [18] - Herczeg et al. (2009), [19] - Long et al. (2017).

a: NR: The existence of a disk has not been reported for this object.

References for spectral type: [20] - Alves de Oliveira et al. (2012), [21] - Luhman (2007), [22] - Luhman (2004), [23] - Lodieu et al. (2018), [24] - Slesnick et al. (2008), [25] - Bihain et al. (2010), [26] - Martín et al. (1996), [27] - Stauffer et al. (1998), [28] - Boudreault & Lodieu (2013), [29] - West et al. (2011), [30] - Manara et al. (2017)

References binary candidates: [31] - Gaia Collaboration et al. (2018)

b: NR: Not reported as a binary candidate in the literature.

2 SAMPLE SELECTION

We have selected a sample of 20 benchmark objects with confirmed membership to open clusters or associations, with known ages, metallicities and distances. We have chosen a sample with photometry and optical spectral types confirming their membership. In the case of the Pleiades and Praesepe, members are not only confirmed by photometry and optical spectroscopy, but also by proper motion (Lodieu et al. 2012b; Boudreault et al. 2012; Bouy et al. 2015). We selected objects to each of the associations or open clusters with magnitude ranging from $J=14.9$ to $J=18.1$ mag, which allow us to obtain spectroscopy of a signal-to-noise of between 4 and 53 in the near-infrared, using exposure times between 40 min and 1.5 h. Our sample have spectral types between M5.5 and L3.5, having at least one target per open cluster or association in each spectral type between M5.5 and L0. To complete our sample in age range, we added three members to the UppSco association, and four from the ChaI region from proposals: 093.C-0109(A) (P.I. Van der Plas), 093.C-0769(A) (P.I. Bonnefoy), and 095.C-0378(A) (P.I. Testi). We list the objects in our sample with their main characteristics in Table 1.

We selected four members of the ChaI region (Prusti et al. 1991; Boulanger et al. 1998; Mamajek et al. 2000; Winston et al. 2012, and references therein). ChaI is a molecular cloud with ongoing star formation due to its young age (~ 2 Myr Luhman 2007), but old enough to have relatively low extinction ($A_V \leq 5$ mag). Roccatagliata et al. (2018) found that ChaI has a double population, one north and one south, with slightly difference distances. The north is at 192.7 ± 0.4 pc, while the southern one is at 186.5 ± 0.7 pc, with nearly solar metallicity ($[Fe/H] = -0.08 \pm 0.04$ dex; Spina et al. 2014). All our ChaI targets lie in the northern cloud, with exception of 2MASS J11123099–765334.

We have three members in our sample that belong to the UppSco association. UppSco (de Zeeuw et al. 1999; Kraus et al. 2008; Pecaut et al. 2012; Lodieu 2013, and references therein) is part of the Scorpius Centaurus association, with an estimated age of 5–10 Myr (Slesnick et al. 2008; Song et al. 2012; Feiden 2016; Pecaut & Mamajek 2016; Rizzuto et al. 2016; Fang et al. 2017), and nearly solar metallicity ($[Fe/H] = 0.02$ dex, Carpenter et al. 2014). Its recent average updated distance from *Gaia* is $d=144 \pm 2$ pc, with a standard deviation of ± 17.2 pc (Fang et al. 2017).

Seven objects of our sample are members of the Pleiades open cluster. The Pleiades (Zapatero Osorio et al. 1997; Bouvier et al. 1998; Moraux et al. 2003; Deacon & Hamblly 2004; Lodieu et al. 2012a, and references therein) is an intermediate age open cluster (132 ± 27 Myr, according to the most recent estimate from Lodieu et al. 2019), with solar metallicity (Soderblom et al. 2009) at a distance of 139.41 ± 0.08 pc (Gaia Collaboration et al. 2018), although more recently, Lodieu et al. (2019) provide a distance of 135.15 ± 0.43 pc. The cluster has low foreground extinction, $E(B-V) = 0.04$ mag, as determined by Breger (1986).

Finally, six of the members of our sample belong to the Praesepe open cluster (Jones & Stauffer 1991; Pinfield et al. 2003; Boudreault et al. 2012; Brandt & Huang 2015, and references therein). The Praesepe is the oldest cluster of our sample, with an age between 590–790 Myr, (Fossati et al. 2008; Delorme et al. 2011; Brandt & Huang 2015; Gossage

et al. 2018; Martín et al. 2018), and a metallicity of $[Fe/H] = 0.12-0.16$ dex (Netopil et al. 2016). Its most updated distance provided by *Gaia* (Gaia Collaboration et al. 2018; Lodieu et al. 2019) is 186.18 ± 0.11 pc. The Praesepe has a low reddening on the line of sight of $E(B-V) = 0.027 \pm 0.04$ (Taylor 2006).

3 OBSERVATIONS AND DATA REDUCTION

Our targets were observed between October 2016 and January 2017, under the proposal number ID: 098.C-0277(A) (P.I. Manjavacas), using the X-shooter spectrograph (Vernet et al. 2011), mounted at the Kueyen (UT2,VLT) telescope at the Paranal Observatory. X-shooter is composed of three arms: UVB (300-550 nm), optical (550-1000 nm) and near-infrared (1000-2500 nm). It was operated in echelle slit nod mode, using the 1.3" slit width for the UVB arm, and the 1.2" slit width for the optical and the near-infrared arms. This setup provides resolutions of ~ 2030 in the UVB, ~ 3360 in the VIS, and ~ 3900 in the near-infrared. The average signal to noise of each spectra in the optical and near-infrared is shown in Table 1 of the Appendix. Observations were performed at the parallactic angle to mitigate the effect of differential chromatic refraction. We moved the object along the slit between two positions following an ABBA pattern with a size of 6 arcsec. The flux expected in the UVB arm is extremely low, therefore we chose not to use spectra taken in this range. Telluric standards were observed before or after every target at similar airmass. Bias, darks and flats were taken every night. Arc frames were taken every second day. The observing log including telluric standard stars and the raw seeing during the observations is shown in Table 1 of the Appendix.

The spectra were reduced using the ESO X-shooter pipeline version 1.3.7. In the reduction cascade, the pipeline deletes the non-linear pixels and subtracts bias in the optical or dark frames in the near-infrared. It generates a guess order from a format-check frame, a reference list of arc line and a reference spectral format table. It refines the guess order table by illuminating the instrument pinhole with a continuum lamp. The master flat frame and the order tables tracing the flat edges are created. Finally, the pipeline determines the instrumental response.

In the case of the near infrared, we extracted the 2D spectrum provided by the pipeline with the `apall` routine in IRAF (Image Reduction and Analysis Facility, Tody 1986, 1993)¹. We used the spectrum of the telluric calibration star of the corresponding science target observed in the same night to correct from instrumental response and remove telluric lines. First, we removed artifacts and cosmic rays from the calibration stars. We also removed the H and He absorption lines from their spectra using a Legendre polynomial fit of the pseudo-continuum around the line. We then derived a response function by dividing the non-flux calibrated clean spectrum of the calibration standard by a black body synthetic spectrum with the same temperature as the telluric

¹ IRAF is distributed by the National Optical Astronomy Observatory, which is operated by the Association of Universities for Research in Astronomy (AURA) under a cooperative agreement with the National Science Foundation

star (Theodossiou & Danezis 1991). Finally, we divided our spectra by the corresponding response function calculated with the spectrum of respective calibration star, eliminating the telluric absorption bands and correcting for the instrumental response simultaneously.

We flux calibrated our near-infrared spectra using the J -band magnitudes given by 2MASS (Two Micron All Sky Survey; Skrutskie et al. 2006) or UKIDSS (UKIRT Infrared Deep Sky Survey; Lawrence et al. 2007) for our targets. We convolved our near-infrared spectra with the J filter transmission curves of 2MASS or UKIDSS, depending on the object. The convolved spectra were integrated over the J -band wavelength range and the results were taken to the observed photometric fluxes. This procedure is affected by the error bars of the J -band magnitudes and the uncertainties introduced during the response correction.

To flux calibrate the optical X-shooter spectra, we calculated a scaling factor in the overlapping wavelengths of the optical and near-infrared spectra (995–1020 nm), to match the optical and the near-infrared data.

In addition, we carried out low-resolution optical spectroscopy with the Optical System for Imaging and low Resolution Integrated Spectroscopy (OSIRIS; Cepa et al. 2000) mounted on the 10.4 m Gran Telescopio Canarias (GTC) in the Roque de Los Muchachos Observatory in La Palma (Canary Islands) under program GTC66-12B (PI Boudreault). We used the R300R grism and a 1.0 arcsec slit with a 2×2 binning of the detector, yielding a spectral resolution of ~ 300 at 680 Å. This configuration shows contamination from the second-order light redwards of 9000 Å. Therefore, we restrain the range of analysis of our spectra to the 5500–9000 Å wavelength range. We observed six members of Praesepe and one member of the Pleiades (see Table 2 in the Appendix for a log of observations) under grey time, spectroscopic conditions, and seeing better than 1.2 arcsec. We offset the object along the slit in case of several exposures. We reduced the optical spectra using standard IRAF packages (Tody 1986, 1993). To summarize, we first subtracted the overscan and removed the flat-field contribution before trimming the images with the `ccdred` package. Then we optimally extracted the spectrum that we calibrated in wavelength using a combination of HgAr, Ne and Xe lamps. To flux calibrate GTC/OSIRIS optical spectra, we followed a similar procedure for the near-infrared data, but we used the Pan-STARRS (Panoramic Survey Telescope and Rapid Response System; Chambers et al. 2016) i -filter. The final Xshooter and OSIRIS spectra are presented in Figures 1, 2, 3 and 4 of the Appendix.

4 ANALYSIS AND RESULTS

4.1 Spectral Types

We aimed at performing a consistent spectral classification of the objects in our sample in the optical and in the near-infrared independently. Within both wavelength ranges, we performed two different classifications: one comparing our spectra to field late-M and early L-type dwarfs published in different spectral libraries, and a second one determined by comparing our sample to young brown dwarf spectra of the same types. For this purpose, we compared our optical

spectra to optical young spectral libraries (Luhman & Mamajek 2010; Luhman et al. 2018; Lodieu et al. 2018), and field brown dwarf spectral libraries (Kirkpatrick et al. 1999), determining the best match to both young and field optical spectra. For the comparison, we degraded the resolution of our X-shooter spectra to the resolution of the corresponding comparison spectra. To determine the best match for each object and wavelength range we used the following expression as in Cushing et al. (2008):

$$G = \sum_{\lambda} \left[\frac{C(\lambda) - \alpha T(\lambda)}{\sigma_c(\lambda)} \right]^2, \quad (1)$$

where $C(\lambda)$ is the spectrum of our object, $T(\lambda)$ is the comparison spectrum, α is a scaling factor that minimises G , and $\sigma_c(\lambda)$ are the uncertainties of the target spectrum.

In Table 2 we summarise the optical and near-infrared spectral types obtained from the best matches. We show the best matches for Praesepe, the Pleiades, USco, and Cha in Figures 1+2, 3+4, 5+6, and 7+8, respectively.

We find a maximum dispersion of ± 2.5 spectral types between the different spectral classifications, for the members of the Praesepe, and for the members of the Chamaelon I association. Differences in spectral classification using different wavelengths and type of objects are expected, as the spectral characteristics of brown dwarfs and low-mass stars evolve with age (i.e. surface gravity). This likely explains why fitting field brown dwarf spectra to younger brown dwarf spectra and vice-versa might provide slightly different spectral types.

In addition, we need to highlight that the three Cha I members (2MASS J11062554–76334, 2MASS J11074656–76151, and 2MASS J11085497–763241), and two Up-pSco members (2MASS J15591135–233800 and 2MASS J16060391–20564) harbours disks (see Table 1 for details). As a consequence, their Spectral Energy Distribution (SED) usually show near or mid-infrared excesses, which might lead to later spectral type estimates.

For the subsequent analysis in this paper, we will adopt as final spectral classification the one provided by the comparison to near-infrared field objects (third column in Table 2). The reason to choose this spectral classification is that most of the flux of the objects in our sample is in this wavelength range. The reason we choose field objects for the spectral classification is that they provide a reasonable fit for most of the object’s near-infrared spectra. In addition, the spectral classification sequence of field low-mass stars and brown dwarfs have been well-defined in the literature so far (Kirkpatrick et al. 1999; Cushing et al. 2005; Burgasser et al. 2006, and references therein), in contrast with the spectral classification for young low-mass stars or brown dwarfs.

4.2 Spectral Characteristics

4.2.1 Pseudo Equivalent Widths of Alkali Lines

Surface gravity has been found to be correlated with the pseudo equivalent widths (pEWs) of the alkali lines (Steele & Jameson 1995; Martín et al. 1996; Gorlova et al. 2003; Cushing et al. 2005; Allers et al. 2007; Allers & Liu 2013; Bonnefoy et al. 2014a, and references therein).

To estimate relative surface gravities of our sample, we

Table 2. List of derived optical and near-infrared spectral types using field and young brown dwarfs.

Num.	Name	Opt SpT field	Opt SpT young	NIR SpT Field	NIR SpT Young
1	UGCS J083748.00+201448.5	M7.0	M5.5	M6.0	M8.0
2	2MASS J08370215+1952074	M6.0	M7.0	M7.5	M8.0
3	UGCS J083654.60+195415.7	M8.0	M7.25	M7.0	M8.0
4	2MASS J08410852+1954018	M8.0	M8.0	M9.0	M8.0
5	2MASS J08370450+2016033	L0.0	L1.0	L0.0	L0.0
6	UGCS J084510.65+214817.0	L1.5	L1.0	L1.5	L2.0
7	2MASS J03484469+2437236	M6.0	M5.5	M6.0	M6.0
8	2MASS J03491512+2436225	M7.0	M6.5	M6.0	M6.0
9	2MASS J03512557+2345214	M6.5	M6.5	M7.0	M7.25
10	2MASS J03443516+2513429	M7.5	M6.5	M7.0	M7.0
11	2MASS J03463425+2350036	L0.0	L1.0	L1.0	L2.0
12	2MASS J03461406+2321565	M7.0	M6.5	M7.0	M6.0
13	2MASS J03541027+2341402	NA	NA	L3.0	L3.0
14	2MASS J15591135-2338002	M7.5	M7.0	M8.5	M7.25
15	2MASS J16060391-2056443	M8.0	M7.5	M8.5	M7.0
16	2MASS J16060629-2335133	L0.0	L1.0	M9.5	M9.0
17	2MASS J11085497-7632410	M7.0	M6.0	M8.0	M6.0
18	2MASS J11123099-7653342	M7.0	M6.5	M7.0	M7.0
19	2MASS J11074656-7615174	M7.0	M6.5	M8.0	M8.0
20	2MASS J11062554-7633418	M6.0	M5.75	M8.0	M6.0

NA: Spectrum not available.

Table 3. List of measured lines in the optical spectra with central wavelength of the line and continuum edges.

Line	λ_{line} (nm)	Continuum 1 (nm)	Continuum 2 (nm)
Li I	670.8	669.0	672.0
H α	656.3	655.0	657.0
Rb I	794.8	792.7	797.5
Na I	818.3	817.7	818.8
Na I	819.5	819.0	819.5
Cs I	852.0	851.0	853.4

measured the pEWs of the following alkali lines in the optical: Rb I (794.8 nm), Na I (818.3 nm), Na I (819.5 nm), and Cs I (852.0 nm). We also measured the Li I line (670.8 nm) and the H α line (656.3 nm). In the near-infrared, we measure the 1169.2 nm, 1177.8 nm, 1243.7 and 1252.9 nm KI lines. These lines are blended with FeH, Fe I, and H₂O features in the *J*-band for objects with spectral types similar to those in our sample, which might constrain the reliability of these features as age indicators. We measured the pEWs using the same pseudo continuum windows as defined in Allers & Liu (2013) for the alkali lines in the near-infrared. For alkali lines in the optical, we use the windows shown in Table 3.

In Figures 1 and 2 we present the pEWs of the alkali lines in the optical and in the near-infrared for objects in our sample with ages from 2 Myr to 590–790 Myr expanding through low-gravity, intermediate gravity and field gravity classes defined in Allers & Liu (2013). In Tables 4, and 5, we present the pEWs measured values for the alkali lines. In the near-infrared, we overplotted field objects (McLean et al. 2003; Cushing et al. 2005), objects that belong to TW Hydrae Association (TWA), young companions (Allers & Liu 2013; Bonnefoy et al. 2014b), young β -dwarfs and γ -dwarfs as a comparison (Allers & Liu 2013). In addition, we include high probability members to open clusters from Martín et al. (2017), those involve five objects from α Persei (90 \pm 10 Myr;

Stauffer et al. 1999; Barrado y Navascués 2004), seven objects from Rho Ophiuchi (0.3 $^{+2.7}_{-0.2}$ Myr; Wilking et al. 2005), two of TWA (10 \pm 3 Myr; Mamajek 2005), 13 objects from Taurus (1.5 \pm 0.5 Myr; Briceño et al. 2002), and 12 from the UppSco association (5–10 Myr).

In the optical we found H α emission at 656.3 nm for at least 12 of the 20 objects, most of them with ages up to 132 \pm 27 Myr, indicating chromospheric activity (Stauffer & Hartmann 1986). In addition, we detect lithium in absorption at 670.8 nm in the four Cha I members and the UppSco objects, indicating that no fusion processes have taken place in the interiors at the age of the association. We do not detect Li in any of the Pleiades members, probably due to the low resolution of the OSIRIS/GTC spectra.

As expected we found that the alkali lines present in the optical spectra (Rb I at 794.8 nm, Na I at 818.3 nm, Na I at 819.5 nm and Cs I at 852.0 nm, see Figure 1) are weaker for younger objects (see blue points and violet stars belonging to targets from UppSco and Cha I, respectively). Members of the Praesepe open cluster and the Pleiades have nearly similar pEWs for the alkali lines, even though the Pleiades (132 \pm 27 Myr) is much younger than the Praesepe (590–790 Myr). That would suggest that gravity does not change much after the age of the Pleiades, and therefore, we can consider that low mass stars and more massive brown dwarfs have significantly approached their final radii after their first \sim 100 Myr. This tendency agrees with predictions of evolutionary models (Baraffe et al. 2015) that estimate a decrease in radii for a dwarf of 60 M_{Jup} by a factor of 4.4 between 1 and 100 Myr. Between 100 Myr and 3 Gyr, the predicted decrease radii is a factor of 1.8, which translates to a change in surface gravity from 3.8 dex for the very young objects to 4.9 dex for objects of around 100 Myr and 5.3 dex for objects older than a few hundred Myr.

In the near-infrared (see Figure 2) we observe that the alkali lines are weaker for younger objects in general. We observe that objects belonging to α Persei (\sim 90 Myr), Pleiades (132 \pm 27 Myr) and Praesepe (590–790 Myr) have similar

Table 4. Equivalent widths in nm for alkali lines, and H- α emission measured in the optical. Negative values indicate lines in emission.

Name	NIR SpT	H α [1]	He I [2]	Li I [2]	Rb I [4]	Na I [5]	Na I [6]	Cs I [7]
UGCS J083748.00+201448.5	M7.0	<0.02	NA	NA	<0.01	NA	NA	NA
2MASS J08370215+1952074	M8.0	-1.79 \pm 0.20	<0.14	<0.15	0.05 \pm 0.02	0.14 \pm 0.01	0.15 \pm 0.01	0.06 \pm 0.01
UGCS J083654.60+195415.7	M8.0	<0.02	NA	NA	<0.02	NA	NA	NA
2MASS J08410852+1954018	M9.0	<0.02	NA	NA	NA	NA	NA	NA
2MASS J08370450+2016033	L0.0	NA	NA	NA	NA	NA	NA	NA
UGCS J084510.65+214817.0	L1.5	NA	NA	NA	NA	NA	NA	NA
2MASS J03484469+2437236	M6.0	-0.75 \pm 0.05	NA	<0.04	0.06 \pm 0.10	0.15 \pm 0.01	0.14 \pm 0.01	0.03 \pm 0.01
2MASS J03491512+2436225	M6.0	-0.97 \pm 0.06	NA	<0.06	0.07 \pm 0.01	0.14 \pm 0.01	0.14 \pm 0.01	0.07 \pm 0.01
2MASS J03512557+2345214	M7.0	-1.14 \pm 0.32	<0.14	<0.58	0.09 \pm 0.03	0.15 \pm 0.01	0.16 \pm 0.02	0.07 \pm 0.02
2MASS J03443516+2513429	M8.5	-0.87 \pm 0.41	-0.37 \pm 0.27	<0.38	0.08 \pm 0.04	0.13 \pm 0.01	0.12 \pm 0.02	0.10 \pm 0.02
2MASS J03463425+2350036	L1.0	NA	NA	NA	NA	NA	NA	NA
2MASS J03461406+2321565	M7.0	-0.89 \pm 0.19	-0.09 \pm 0.15	<0.14	0.09 \pm 0.02	0.13 \pm 0.01	0.17 \pm 0.01	0.07 \pm 0.01
2MASS J03541027+2341402	L3.0	NA	NA	NA	NA	NA	NA	NA
2MASS J15591135-2338002	M8.5	-4.93 \pm 0.03	-0.17 \pm 0.03	0.04 \pm 0.01	0.06 \pm 0.01	0.09 \pm 0.01	0.08 \pm 0.01	0.06 \pm 0.01
2MASS J16060391-2056443	M8.5	-12.15 \pm 0.07	-0.09 \pm 0.01	0.02 \pm 0.01	0.06 \pm 0.01	0.07 \pm 0.01	0.07 \pm 0.01	0.03 \pm 0.01
2MASS J16060629-2335133	M9.5	-2.16 \pm 0.30	<0.02	0.35 \pm 0.10	0.13 \pm 0.06	0.12 \pm 0.01	0.13 \pm 0.02	0.09 \pm 0.04
2MASS J11085497-7632410	M6.0	-4.16 \pm 0.01	-0.024 \pm 0.10	<0.01	<0.02	0.06 \pm 0.01	0.07 \pm 0.01	0.04 \pm 0.01
2MASS J11123099-7653342	M7.0	-1.32 \pm 0.08	-0.15 \pm 0.06	<0.07	0.04 \pm 0.01	0.09 \pm 0.01	0.05 \pm 0.02	0.06 \pm 0.01
2MASS J11074656-7615174	M8.0	-2.26 \pm 0.03	<0.02	<0.05 \pm 0.02	0.04 \pm 0.01	0.08 \pm 0.01	0.06 \pm 0.01	0.03 \pm 0.01
2MASS J11062554-7633418	M8.0	-1.96 \pm 0.01	NA	0.04 \pm 0.01	0.03 \pm 0.01	0.07 \pm 0.01	0.03 \pm 0.01	0.04 \pm 0.01

Lines wavelengths: [1] H α : 656.3 nm - [2] He I: 667.7 nm - [3] Li I: 670.8 nm - [4] Rb I: 794.8 nm - [5] Na I: 818.3 nm - [6] Na I: 819.5 nm - [7] Cs I: 852.0 nm

Table 5. Equivalent widths in nm for alkali lines measured in the near-infrared.

Name	NIR SpT	KI (1169 nm)	KI (1177 nm)	KI (1243 nm)	KI (1253 nm)	GS ^{a,b}	OC/A ^c
UGCS J083748.00+201448.5	M6.0	0.35 \pm 0.02	0.42 \pm 0.04	0.19 \pm 0.02	0.25 \pm 0.01	00-0 / FLD-G	Praesepe
2MASS J08370215+1952074	M7.5	0.21 \pm 0.02	0.48 \pm 0.03	0.31 \pm 0.01	0.30 \pm 0.01	11-1 / INT-G	Praesepe
UGCS J083654.60+195415.7	M7.0	0.33 \pm 0.01	0.52 \pm 0.05	0.79 \pm 0.04	0.40 \pm 0.02	11-1 / INT-G	Praesepe
2MASS J08410852+1954018	M9.0	0.72 \pm 0.04	0.69 \pm 0.05	0.63 \pm 0.01	0.39 \pm 0.02	01-1 / FLD-G	Praesepe
2MASS J08370450+2016033	L0.0	0.54 \pm 0.01	0.63 \pm 0.04	0.56 \pm 0.04	0.53 \pm 0.02	11-1 / INT-G	Praesepe
UGCS J084510.65+214817.0	L1.5	0.91 \pm 0.01	0.75 \pm 0.05	0.47 \pm 0.04	0.62 \pm 0.03	01-1 / FLD-G	Praesepe
2MASS J03484469+2437236	M6.0	0.18 \pm 0.01	0.17 \pm 0.03	0.07 \pm 0.02	0.18 \pm 0.01	02-1 / INT-G	Pleiades
2MASS J03491512+2436225	M6.0	0.18 \pm 0.01	0.33 \pm 0.02	0.11 \pm 0.02	0.20 \pm 0.01	00-1 / FLD-G	Pleiades
2MASS J03512557+2345214	M7.0	0.30 \pm 0.01	0.50 \pm 0.03	0.11 \pm 0.04	0.39 \pm 0.02	00-0 / FLD-G	Pleiades
2MASS J03443516+2513429	M7.0	0.39 \pm 0.01	0.54 \pm 0.04	0.50 \pm 0.02	0.39 \pm 0.01	00-0 / FLD-G	Pleiades
2MASS J03463425+2350036	L1.0	0.63 \pm 0.01	0.69 \pm 0.04	0.58 \pm 0.04	0.52 \pm 0.03	11-1 / INT-G	Pleiades
2MASS J03461406+2321565	M7.0	0.26 \pm 0.01	0.30 \pm 0.02	0.13 \pm 0.02	0.24 \pm 0.01	12-1 / INT-G	Pleiades
2MASS J03541027+2341402	L3.0	0.80 \pm 0.08	0.75 \pm 0.02	0.56 \pm 0.06	0.30 \pm 0.04	11-2 / INT-G	Pleiades
2MASS J15591135-2338002	M8.5	0.15 \pm 0.02	0.23 \pm 0.02	<0.02	0.10 \pm 0.01	22-2 / VL-G	UpSco
2MASS J16060391-2056443	M8.5	0.12 \pm 0.01	0.22 \pm 0.01	NA	0.06 \pm 0.01	22- / VL-G	UpSco
2MASS J16060629-2335133	M9.5	0.24 \pm 0.01	0.27 \pm 0.04	0.10 \pm 0.03	0.14 \pm 0.02	22-2 / VL-G	UpSco
2MASS J11085497-7632410	M8.0	0.03 \pm 0.01	0.17 \pm 0.01	NA	<0.03	22- / VL-G	ChaI
2MASS J11123099-7653342	M7.0	0.09 \pm 0.01	0.02 \pm 0.04	<0.03	<0.03	22-2 / VL-G	ChaI
2MASS J11074656-7615174	M8.0	0.04 \pm 0.01	0.18 \pm 0.01	NA	NA	22- / VL-G	ChaI
2MASS J11062554-7633418	M8.0	0.05 \pm 0.01	0.17 \pm 0.02	0.04 \pm 0.01	<35.74	222- / VL-G	ChaI

a: GS: Gravity scores calculated as in Allers & Liu (2013). b: Gravity scores are ordered according to the alkali line that they correspond to. The dash symbol indicates that none gravity score can be determined with that particular line. c: OC/A: Open Cluster/Association to which the target belongs to.

pEWs for all for KI alkali lines, confirming the tendency found in the optical that suggests that gravity does not increase significantly after \sim 100 Myr. The M and L dwarfs belonging to the Pleiades, have slightly weaker pEWs in the near-infrared than field objects.

In addition, we observe that the increase of the pEWs is steeper for objects with spectral type later than M8, where the increases in pEWs quadruple from the youngest to the oldest objects (see Section 4.2.2). Therefore, only for objects later than M8, the pEWs of the alkali lines on the J -band might be useful age indicators. An extra challenge when we aim to use alkali lines in the J -band as age tracers is the existence of remaining features from the telluric correction,

and the blending of these lines with some other spectroscopic features, like the FeH, FeI and H₂O that might introduce extra noise in the measurements of those lines. We find that the best line as gravity/age tracer in the near-infrared is the KI line at 1253 nm, in agreement with Martín et al. (2017) and Lodieu et al. (2018), for which the pEWs have uncertainties between 5–10%.

Finally, we obtained the gravity scores corresponding to each object as described by Allers & Liu (2013). For each near-infrared spectral type, they defined intervals of values of pEWs of the KI lines in the J -band that correspond to very low-gravity (VL-G), intermediate gravity (INT-G) and field gravity (FLD-G) objects (see Table 10 of Allers & Liu

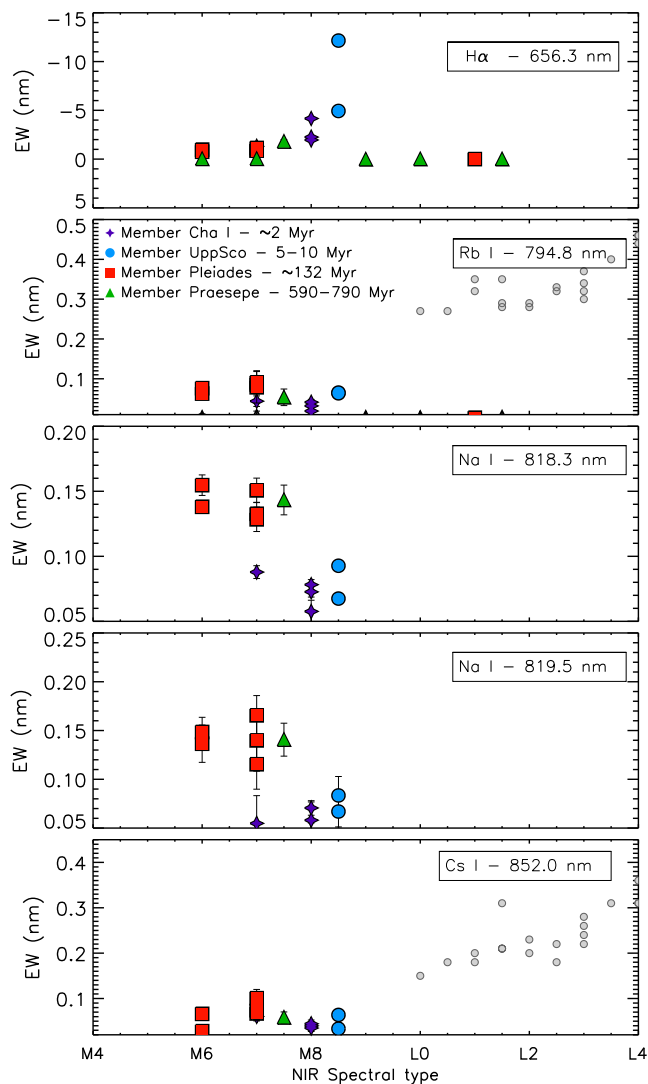


Figure 1. Equivalent widths of the detected alkali lines, and the H- α line in the optical for our benchmark objects with different ages: purple stars, blue circles, red squares, and green triangles. Grey circles represent other L-dwarfs from Chiu et al. (2006), Golimowski et al. (2004), and Knapp et al. (2004).

2013). A gravity score of "0" is the index of an object classified as an old field dwarf. A score of "1" indicates intermediate surface gravity. Finally, a score index of "2" means that the pEW or index indicates low surface gravity. The values of the pEW or indices that define each category can be found in Tables 9 and 10 from Allers & Liu (2013). The final gravity score is calculated as a median of all the scores. The field gravity objects have a final score of ≤ 0.5 . The intermediate gravity objects have a median gravity score of 1. Finally, objects with a median gravity of ≥ 1.5 belong to the very low gravity object category. In Table 5, we show the gravity scores obtained for our sample.

The gravity scores classified correctly very low gravity objects (belonging to UppSco and Cha I, respectively), but Praesepe and Pleiades objects have mixed field and interme-

diated surface gravity classifications (see Table 5). Thus, these gravity scores do not always predict the surface gravity expected for the members to each of the clusters/associations that we consider in this study.

4.2.2 Correlation between ages and alkali lines in the near-infrared

In Figure 3, we plot the age of objects in our sample in logarithmic scale vs the pEWs of the KI lines in the J -band. We add objects with spectral types from M5.5 and L3.5 with well-determined ages from Martín et al. (2017). As suggested by visual inspection in Figures 1 and 2, the pEWs of the alkali lines increase from earlier to later spectral types. Within each spectral type, their pEWs increase from lower to higher surface gravity. We calculate a Kendall correlation index to probe correlation between the pEWs for the KI lines in the J -band and the age. We obtained Kendall correlations around 0.63 with significances very close to 0, indicating that there is a moderate correlation between the pEWs of the alkali lines in the J -band and the age.

We fitted a first order polynomial that tentatively relates $\log(\text{Age})$ with pEWs of all the KI lines in the J -band at 1169 nm, 1177 nm, 1243 nm and 1253 nm. We do not investigate fits with higher order polynomials as the dispersion of the pEWs is remarkable and we just intend to derive a tentative relation between age and pEWs of the KI lines in the J -band. We use the IDL routine `poly_fit.pro`. This routine performs a least-square fit with optional weighting and returns a vector with the coefficients and its χ^2 . We added the pEWs vs age plot with the pEWs measured by Martín et al. (2017), thus, we have M5.5 to L3.5 dwarfs with ages from $0.3^{+2.5}_{-0.2}$ Myr (ρ Oph) to 590–790 Myr (Praesepe), covering the whole VL-G, INT-G and FLD-G classification. In Table 6 we show the best matching first order polynomial for M5.5–M7.0 and M7.0–M8.5 spectral types. We do not provide polynomials for the rest of the spectral types due to the lack of objects within those ranges of spectral types.

4.2.3 Spectral Indices and Gravity Scores

We calculated the FeH_J, KI_J, FeH_z, VO_z and H -cont spectral indices to estimate surface gravity as defined in Allers & Liu (2013). The FeH_J index at 1200 nm has been found to be correlated with surface gravity (McGovern et al. 2004). The KI_J measures the depth of the KI doublet at 1250 nm. The VO band disappears as surface gravity increments with age due to condensation effects (Lodders 2002). The shape of the continuum of the H -band has been found to be affected by surface gravity (Borysow et al. 1997; Bowler et al. 2012). For young objects, the shape of the H -band is usually triangular-shaped, thus the H -cont index measures how much the blue-end of the H -band deviates from a straight line. The H -cont is small for high gravity objects, and close to 1 for young objects.

Using the method presented in Allers & Liu (2013) we determined the spectral indices to determine the gravity scores from the FeH_J, KI_J, FeH_z, VO_z and H -cont indices. Nonetheless, it is important to note that Lodieu et al. (2017) identified the H -cont index as the most sensitive to gravity (or age) after testing several indices in a sample of field L

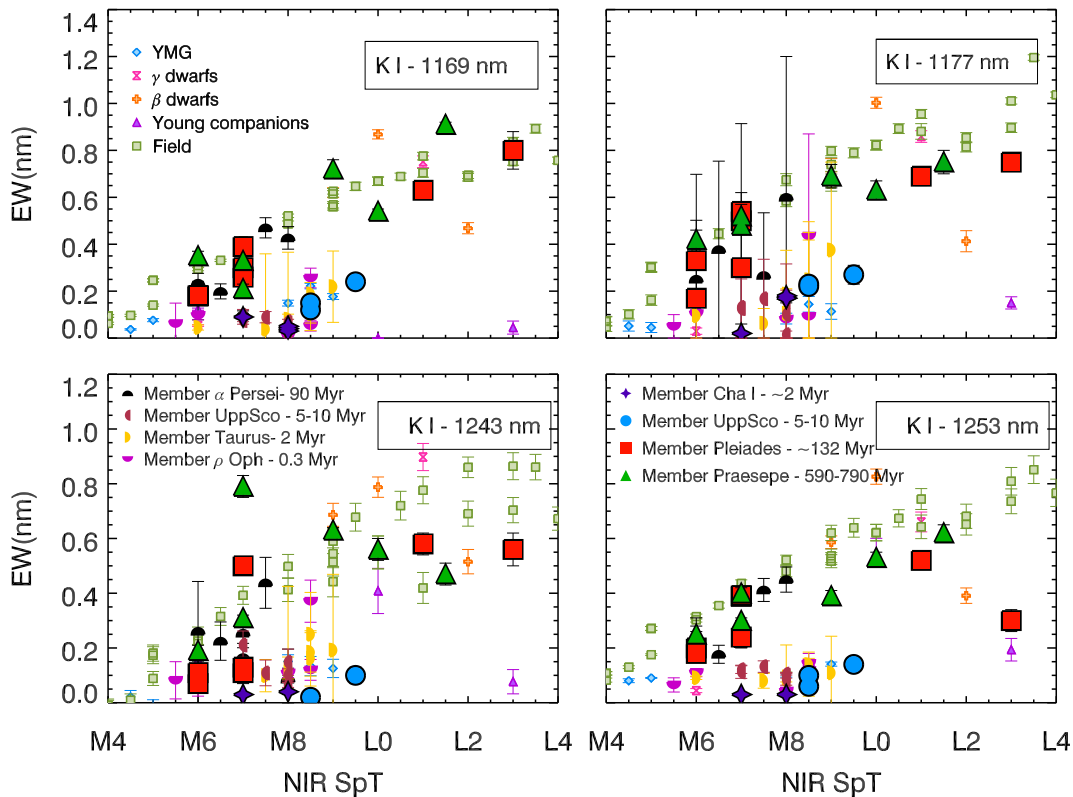


Figure 2. Equivalent widths of the detected alkali lines in the near-infrared for our benchmark objects with different ages: purple stars, blue circles, red squares, and green triangles. We overplot field objects (McLean et al. 2003; Cushing et al. 2005), objects that belong to TW Hydrae Association (TWA), young companions (Allers & Liu 2013; Bonnefoy et al. 2014b), young β -dwarfs and γ -dwarfs as a comparison (Allers & Liu 2013). We include the pEWs published by Martín et al. (2017) of confirmed members of α Persei (90 Myr, black half upper circle), of UppSco (5–10 Myr, red half left circles), of Taurus (2 Myr, yellow half right circles), and from ρ Ophiuchi (0.3 Myr, pink half down circles).

Table 6. Tentative linear relation between pEW of all the alkali lines and $\log_{10}(\text{Age})$ (Myr) plots as shown in Figure 3.

SpT range	Polynomial		χ^2_{red}	Kendall- τ coeff.	significance
	c_0	c_1			
M5.5–M7.0	0.1383 ± 0.0177	8.9477 ± 0.1321	339.4	0.62	$1.94e-5$
M7.0–M8.5	-0.1809 ± 0.0046	8.7026 ± 0.0462	987.5	0.63	0.0

The polynomials are defined as: $\log_{10}(\text{Age}) = c_0 + c_1 \times \text{pEW}$

dwarfs, young β and γ L dwarfs and L dwarfs members to the UppSco association. We show the gravity scores obtained for the spectral indices for our objects in Table 7.

In Table 8 we summarise the final gravity scores given by the alkali lines and the gravity indices from Allers & Liu (2013) for each object. Combining all gravity indicators, we obtained in general a consistent gravity classification with the age of the cluster or association. Nonetheless, we note that three of the six Praesepe members would be classified as INT-G instead of FLD-G with the spectral indices and gravity scores. Similarly, one member of the Pleiades obtained a VL-G classification, and two of them obtained a FLD-G classification, which would not correspond to the expected gravity classification for the Pleiades.

4.3 Age sequences

We present the age sequences of M7.0–M8.5 brown dwarfs and low mass stars from our X-shooter sample with wavelengths from 0.6 to 2.5 μm from 2 Myr (corresponding to the VL-G gravity class) to 590–790 Myr (corresponding to the FLD gravity class). We degraded the resolution of our spectra to $R \sim 700$ to reduce their noise. Their flux is normalised at 1.226 μm . We applied a positive shift to the spectra to be able to overplot all the age sequence in the same plot. In Figure 5, we compare the optical and the J , H and K bands spectra of 2MASS J11074656–7615174 (M8.0 Cha I member, age ~ 2 Myr), 2MASS J16060391–2056443 (M8.5 UppSco member, 5–11 Myr), 2MASS J035125+23452 (M7, Pleiades

Table 7. Gravity scores for our sample derived from spectral indices defined in the literature (Allers & Liu 2007).

Name	SpT	FeH _J	KI _J	<i>H</i> -cont	FeH _z	VO _z	GS ^a	Member
UGCS J083748.00+201448.5	M6.0	1.042±0.001	1.051±0.001	0.956±0.002	0.873±0.002	1.038±0.002	1002- / FLD-G	Praesepe
2MASS J08370215+1952074	M7.5	1.038±0.001	1.067±0.001	0.908±0.005	1.031±0.001	1.034±0.002	2002- / INT-G	Praesepe
UGCS J083654.60+195415.7	M7.0	1.042±0.001	1.075±0.002	0.943±0.005	0.942±0.003	1.061±0.003	2002- / INT-G	Praesepe
2MASS J08410852+1954018	M9.0	1.056±0.001	1.092±0.002	1.055±0.006	0.922±0.003	1.039±0.003	2002- / INT-G	Praesepe
2MASS J08370450+2016033	L0.0	1.091±0.002	1.111±0.004	0.891±0.001	1.102±0.004	1.152±0.004	20200 / FLD-G	Praesepe
UGCS J084510.65+214817.0	L1.5	1.105±0.002	1.118±0.003	0.892±0.003	0.956±0.003	1.165±0.004	20000 / FLD-G	Praesepe
2MASS J03484469+2437236	M6.0	1.031±0.001	1.021±0.001	0.993±0.002	1.003±0.001	1.023±0.002	2202- / VL-G	Pleiades
2MASS J03491512+2436225	M6.0	1.043±0.001	1.037±0.001	0.951±0.001	1.042±0.001	1.020±0.002	1101- / INT-G	Plei
2MASS J03512557+2345214	M7.0	1.067±0.002	1.071±0.002	0.954±0.001	1.081±0.001	1.101±0.002	1001- / FLD-G	Pleiades
2MASS J03443516+2513429	M7.0	1.071±0.002	1.062±0.002	0.935±0.001	1.057±0.001	1.108±0.003	1001- / FLD-G	Pleiades
2MASS J03463425+2350036	L1.0	1.093±0.002	1.098±0.004	0.937±0.003	0.899±0.005	1.287±0.006	21022 / INT-G	Pleiades
2MASS J03461406+2321565	M7.0	1.058±0.001	1.034±0.002	0.954±0.001	1.029±0.001	1.062±0.002	1202- / INT-G	Pleiades
2MASS J03541027+2341402	L3.0	1.067±0.002	1.069±0.002	0.853±0.004	0.819±0.002	1.341±0.002	22022 / VL-G	Pleiades
2MASS J15591135-2338002	M8.5	1.016±0.001	1.037±0.001	0.978±0.003	1.040±0.002	1.067±0.002	2212- / VL-G	UpSco
2MASS J16060391-2056443	M8.5	1.013±0.001	1.022±0.001	0.996±0.002	1.041±0.001	1.081±0.002	2222- / VL-G	UpSco
2MASS J16060629-2335133	M9.5	1.059±0.002	1.057±0.002	0.955±0.002	1.00±0.001	1.180±0.003	2112- / VL-G	UpSco
2MASS J11085497-7632410	M8.0	1.008±0.001	1.006±0.001	0.958±0.002	0.986±0.001	1.031±0.001	2202- / VL-G	Cha I
2MASS J11123099-7653342	M7.0	1.017±0.001	1.022±0.001	0.974±0.002	1.005±0.001	1.084±0.001	2202- / VL-G	Cha I
2MASS J11074656-7615174	M8.0	1.030±0.001	1.005±0.001	0.977±0.002	1.006±0.001	1.021±0.001	2222- / VL-G	Cha I
2MASS J11062554-7633418	M8.0	1.023±0.001	1.008±0.001	0.956±0.001	1.001±0.001	1.010±0.001	2202- / VL-G	Cha I

a: GS: Gravity scores calculated as in Allers & Liu (2013)

Table 8. Summary of gravity scores provided by the alkali lines and gravity indices.

Name	NIR SpT	GS ^a	OC/A ^c
UGCS J083748.00+201448.5	M6.0	00-01002- / FLD-G	Praesepe
2MASS J08370215+1952074	M7.5	11-12002- / INT-G	Praesepe
UGCS J083654.60+195415.7	M7.0	11-12002- / INT-G	Praesepe
2MASS J08410852+1954018	M9.0	010012002- / FLD-G	Praesepe
2MASS J08370450+2016033	L0.0	11-120200 / INT-G	Praesepe
UGCS J084510.65+214817.0	L1.5	01-120000 / FLD-G	Praesepe
2MASS J03484469+2437236	M6.0	02-12202- / INT-G	Pleiades
2MASS J03491512+2436225	M6.0	00-11101- / INT-G	Pleiades
2MASS J03512557+2345214	M7.0	00-001001- / FLD-G	Pleiades
2MASS J03443516+2513429	M7.0	00-011001- / FLD-G	Pleiades
2MASS J03463425+2350036	L1.0	11-121022 / INT-G	Pleiades
2MASS J03461406+2321565	M7.0	12-11202- / INT-G	Pleiades
2MASS J03541027+2341402	L3.0	11-222022 / VL-G	Pleiades
2MASS J15591135-2338002	M8.5	22-22212- / VL-G	UpSco
2MASS J16060391-2056443	M8.5	22- -2222- / VL-G	UpSco
2MASS J16060629-2335133	M9.5	22-222112- / VL-G	UpSco
2MASS J11085497-7632410	M8.0	22- -2202- / VL-G	Cha I
2MASS J11123099-7653342	M7.0	22-22202- / VL-G	Cha I
2MASS J11074656-7615174	M8.0	22- -2222- / VL-G	Cha I
2MASS J11062554-7633418	M8.0	222-2202- / VL-G	Cha I

a: GS: Gravity scores calculated as in Allers & Liu (2013). c: OC/A: Open Cluster/Association to which the target belongs to.

member, age~137 Myr), and 2MASS J08372.13+195207.4 (M7.5, member to the Praesepe, 590–790 Myr).

In Figure 5, we observe the following evolution of spectral characteristics of M7-M8 dwarfs from younger to older age: in the optical, we do not observe a clear tendency for the TiO (0.71, 0.77 and 0.79 μm), and VO (0.74, 0.76 and 0.84 μm) molecular bands with age, as well as the alkali lines (RbI at 0.794 μm , NaI at 0.818 and 0.819 μm , and CsI at 0.852 μm). Allers & Liu (2013) claimed that VO varies slightly with surface gravity for M-dwarfs at 1.06 μm , but much less than for L-dwarfs. In the near-infrared, we observe that in the *J*-band the KI alkali lines doublets (1.169 and 1.177 μm , 1.243 and 1.253 μm) increase their pEW with age

(i.e. increase of surface gravity). In the *H*-band, the FeH (1.59 μm) absorption appears deeper with age.

4.4 Spectral type-colour diagram

We plot the near-infrared spectral types of our targets, objects with well-constrained ages from Martín et al. (2017), and members to young moving groups from Faherty et al. (2016) versus their *J* – *W*2 colour in Figure 6. Faherty et al. (2016) targets are classified with gravity classes corresponding approximately to intermediate gravity (β) and low gravity objects (γ and δ), respectively. We overplot field dwarfs from Dupuy & Liu (2012) as a comparison. In addition, we

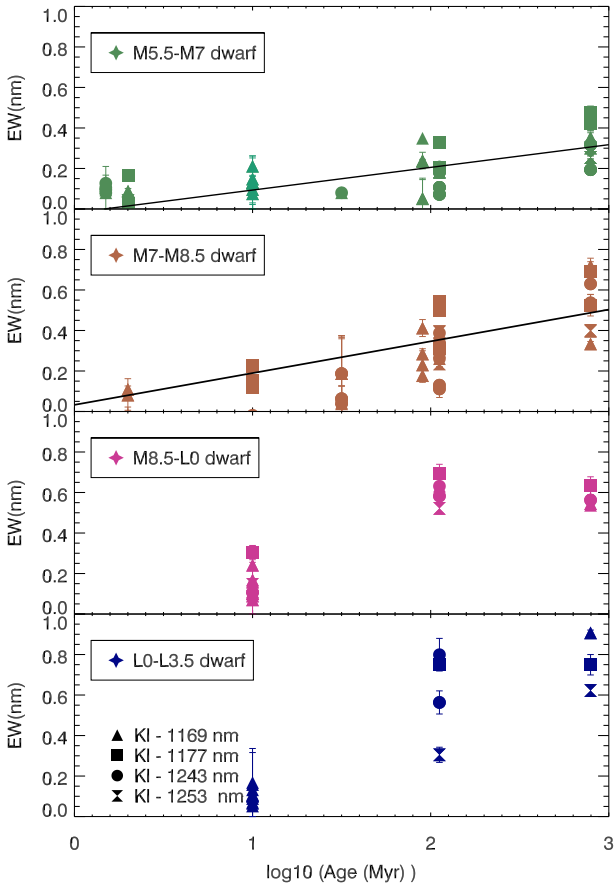


Figure 3. Age versus pEWs of the K I alkali lines in the J -band (line at 1169 nm as triangles, line at 1177 nm as squares, line at 1243 nm as circles, and line at 1253 nm as hourglass) of objects in our sample and members of α Persei, of UppSco, of Taurus, and from ρ Ophiuchi from Martín et al. 2017.

overplot as a blue solid line the spectrophotometric relation of Dupuy & Liu (2012) valid for field dwarfs with its associated rms (dashed lines).

We observe that Cha I, ρ Ophiuchi, Taurus and some UppSco members, all below ~ 10 Myr, lie above the mean $J - W2$ colours for field M and L dwarfs. We observe that objects from Faherty et al. (2016) with spectral types earlier than L0 do not show in general extremely red $J - W2$ colours. In addition, most of their objects with later spectral types show red colours independently of their gravity classification. This fact suggests that, whatever is the cause for red colours in members of young moving groups, it is likely not a direct indication of the age of the source. In addition, it is important to note that the ages of the sample in Faherty et al. (2016) are estimated using the BANYAN tool (Malo et al. 2013; Gagné et al. 2014) that provides the probability of one object to belong to a young moving group, and thus it has a determined age. The results given by the BANYAN tool should be interpreted with caution, and the resulting

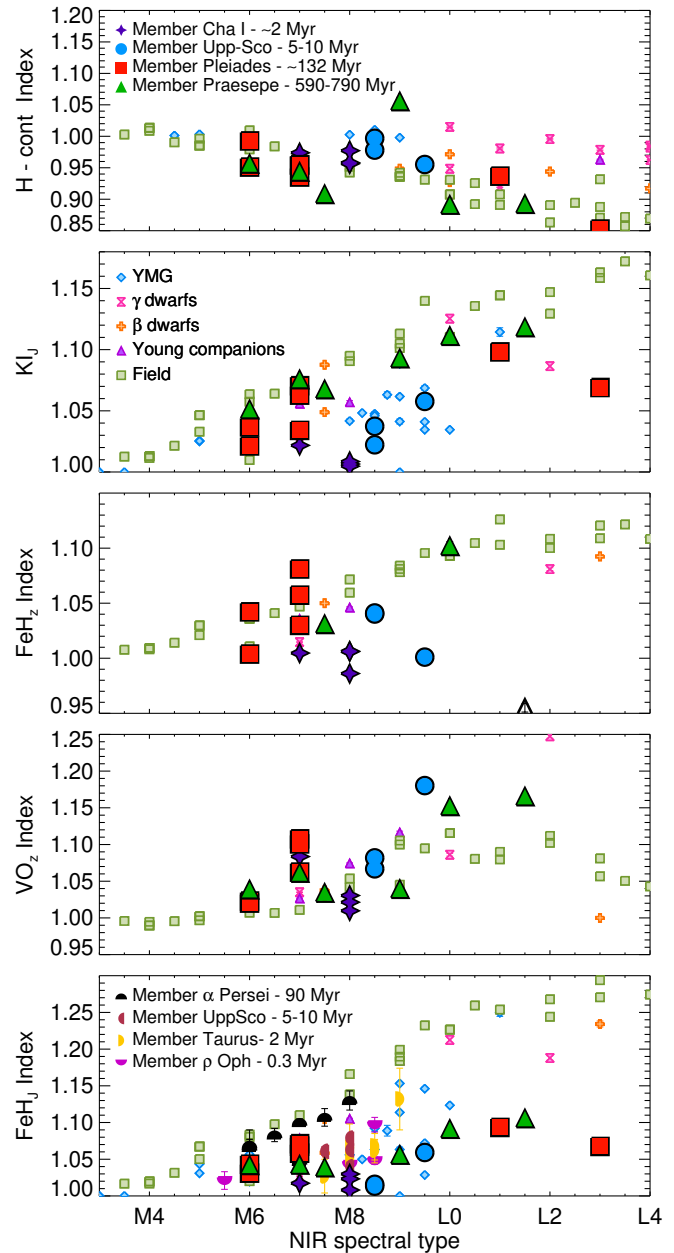


Figure 4. FeH_J , KI_J and H -continuum indices from Allers & Liu (2013) for objects in our sample. We overplot field objects (McLean et al. 2003; Cushing et al. 2005), members to TW Hydrae Association (TWA), young companions (Allers et al. 2007; Bonnefoy et al. 2014b), young β -dwarfs and γ -dwarfs as a comparison (Allers et al. 2007). We include the value of the FeH index for members of Alpha Persei, of UppSco, of Taurus, and from Rho Ophiuchi (Martín et al. 2017)

ages from that tool should be further supported by other indications of young age².

In Figure 7, we plot ages from 0.3 to 590–790 Myr in logarithmic scale, versus $J - W2$ colour for four ranges of

² Further details can be found in: <http://www.astro.umontreal.ca/~gagne/banyanII.php>

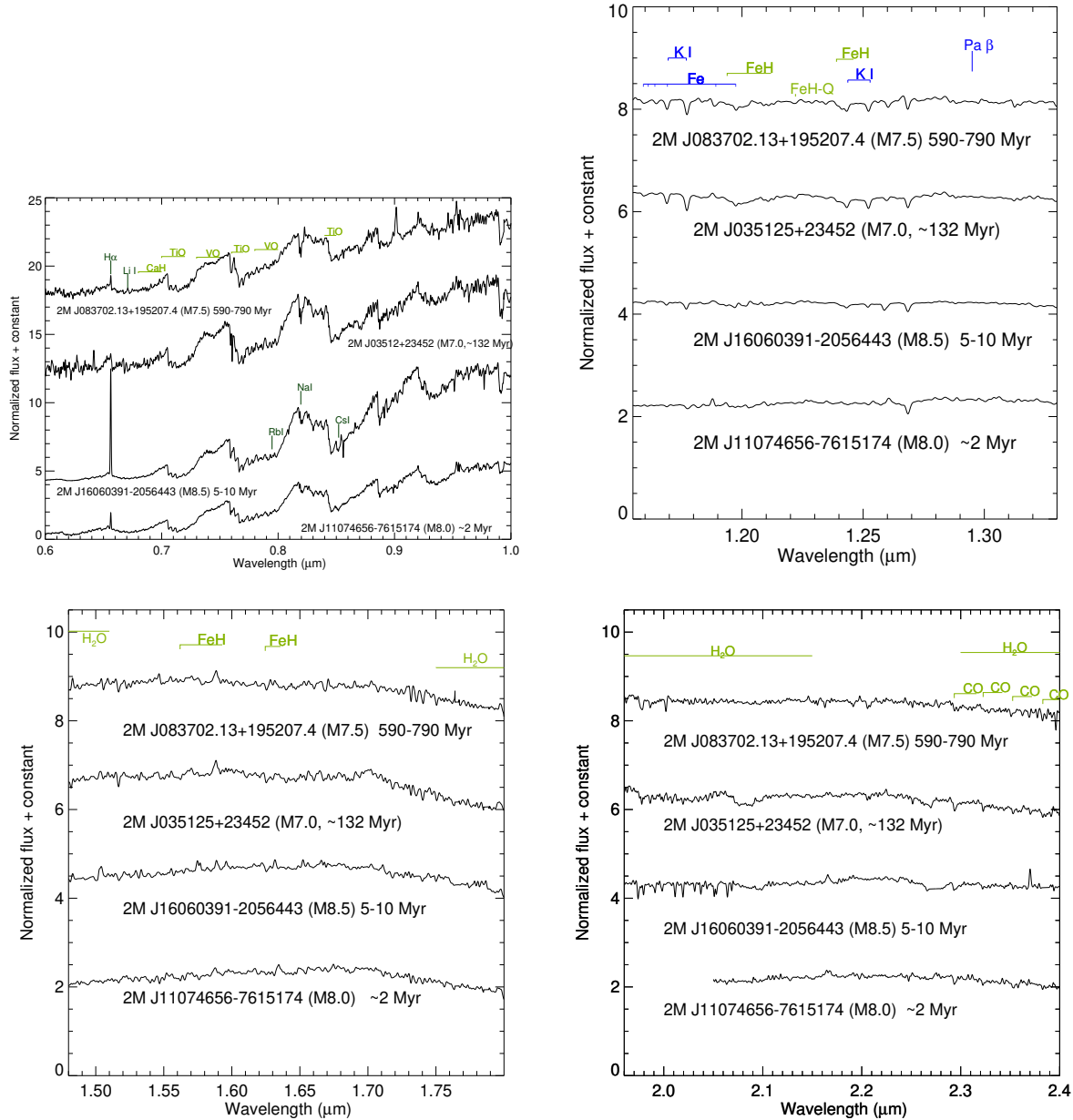


Figure 5. Age sequence of spectra in the optical and near-infrared of M7.0–M8.0 dwarfs with ages from 2 Myr to 790 Myr. The spectral characteristics of M7.0–M8.0 dwarfs are very similar for very young and intermediate age objects.

spectral types: M5.5–M7, M7–M8.5, M8.5–L0 and L0–L3.5. We observe that in general colours of brown dwarfs and low-mass stars are bluer when increasing age. Furthermore, in average, after 10 Myr, the average $J - W2$ colour is similar to the $J - W2$ for objects that are 590–790 Myr old for objects with a similar spectral type. In Table 9, we summarise the Kendall τ coefficient that show the moderate anticorrelation between $J - W2$ red colour and age, with τ values between -0.72 for M5.5–M7.0 spectral types, to -0.54 for L0.0–L3.5 spectral types. The fact that the red colours do not evolve significantly after 10 Myr suggests that the reddening we observe might be due to circumstellar disks, that can survive up to 10 Myr (Carpenter et al. 2006), at least for objects with the spectral types we consider in this work (M6.0–L3.0).

Other alternative explanations for the red colours of some brown dwarfs include the existence of ring structures around these objects (Zakhochay et al. 2017), extinction through the star forming region, a viewing angle with inclinations $>20^\circ$ (Vos et al. 2017), or the presence of sub-micron particle grains in the atmosphere of L dwarfs, which are probably not included in brown dwarf cloud models with the correct number of particles and opacities (Marocco et al. 2014; Hirakawa et al. 2016; Bonnefoy et al. 2016).

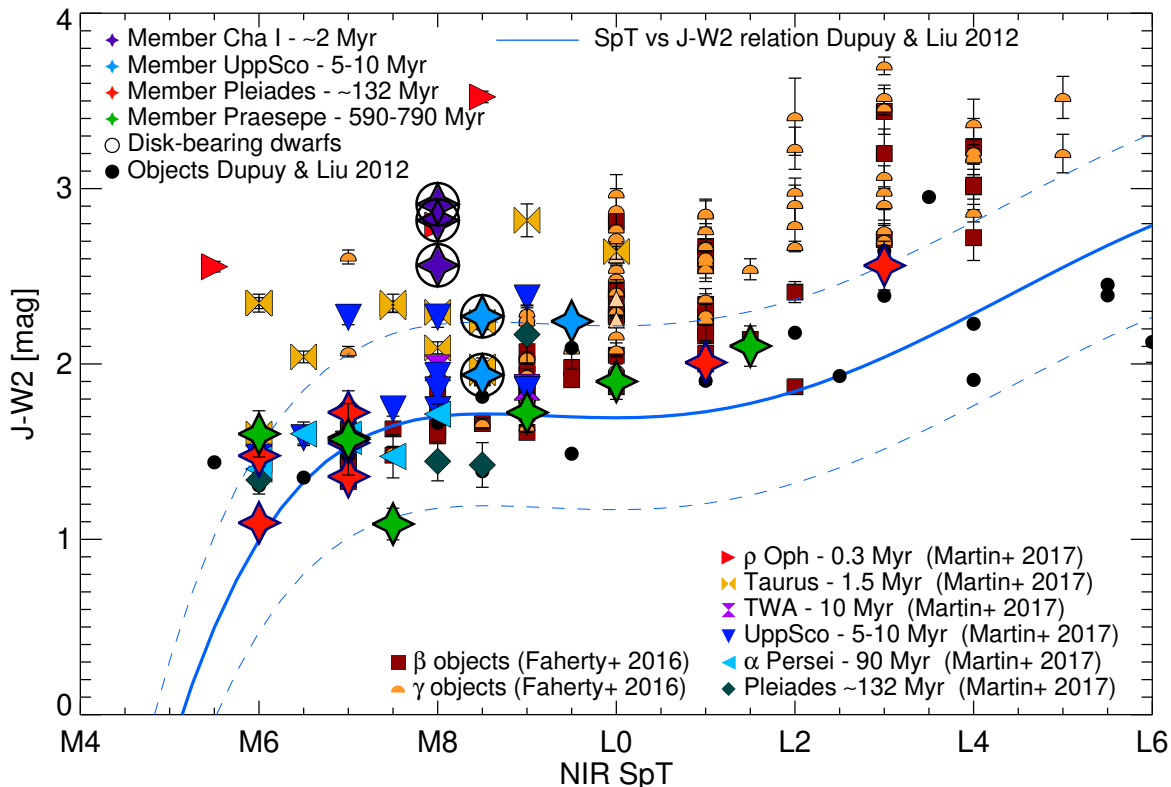


Figure 6. Spectral type vs $J-K$ colour for our sample, dwarfs from Dupuy & Liu (2012), objects with well-determined ages from Martín et al. (2017), and objects members of young moving groups from Faherty et al. (2016). We overplot circles over the targets that bear disks. We overplot with a blue line the spectral-photometric relationship from Dupuy & Liu (2012) for field dwarfs with its typical rms marked with a dashed blue line. We observe that only dwarfs with ages smaller than 10 Myr show $J-K$ red colour, lying above the upper rms line.

Table 9. Kendall coefficients indicating the correlation between to $J - W2$ and $\log_{10}(\text{Age (Myr)})$ plots as shown in Figure 7.

SpT range	Kendall- τ coefficients	significance
M5.5–M7.0	−0.72	1.8e−4
M7.0–M8.5	−0.69	1.8e−7
M8.5–L0.0	−0.54	1.5e−2
L0.0–L3.5	−0.54	1.5e−2

5 PHYSICAL PARAMETERS OF OUR SAMPLE

Due to the age-mass degeneration for brown dwarfs, it is challenging to estimate the ages, masses, radii, and gravities of brown dwarfs. Nevertheless, if we know the ages, we are able to break the age-mass degeneracy and provide a complete physical characterisation of our sample using evolutionary models for low-mass stars and brown dwarfs. This is the aim of this Section.

5.1 Bolometric luminosity and bolometric correction

We have optical and near-infrared spectroscopy from X-shooter, or flux-calibrated optical spectroscopy from OSIRIS, and mid-infrared photometry from the WISE cat-

alog ($W1$ and $W2$) for the all the objects in our sample, which allow us to calculate the bolometric luminosity (L_{bol}), and the bolometric corrections in J - and K -band (BC_J and BC_K). We do not calculate L_{bol} for objects with detected disks: three ChaI members (2MASS J11062554–7633418, 2MASS J11074656–7615174, 2MASS J11085497–7632410), and two UppSco members (2MASS 15591135–23380002, and 2MASS J16060391–2056443).

To calculate the L_{bol} , we employed the method presented in Filippazzo et al. (2015), doing a linear interpolation to fill in the gaps left between 0 flux at $0 \mu\text{m}$, and the X-shooter optical flux calibrated spectra. In case we did not have optical spectrum for the source, we fill in the optical wavelengths using its Pan-STARRS optical photometry. Similarly, we interpolate the water bands at $1.4 \mu\text{m}$ and at $1.8 \mu\text{m}$, and the gap between the X-shooter spectra in the near-infrared and the WISE photometry, $W1$ and $W2$. Finally, we interpolate linearly between the reddest WISE photometric point available and the $1000 \mu\text{m}$, following the procedure of Filippazzo et al. (2015). To calculate the bolometric luminosity of each source we applied the equation:

$$L_{\text{bol}} = 4\pi d^2 \int_{0\mu\text{m}}^{1000\mu\text{m}} F_{\lambda} d\lambda \quad (2)$$

where F_{λ} is the calibrated flux density in units of

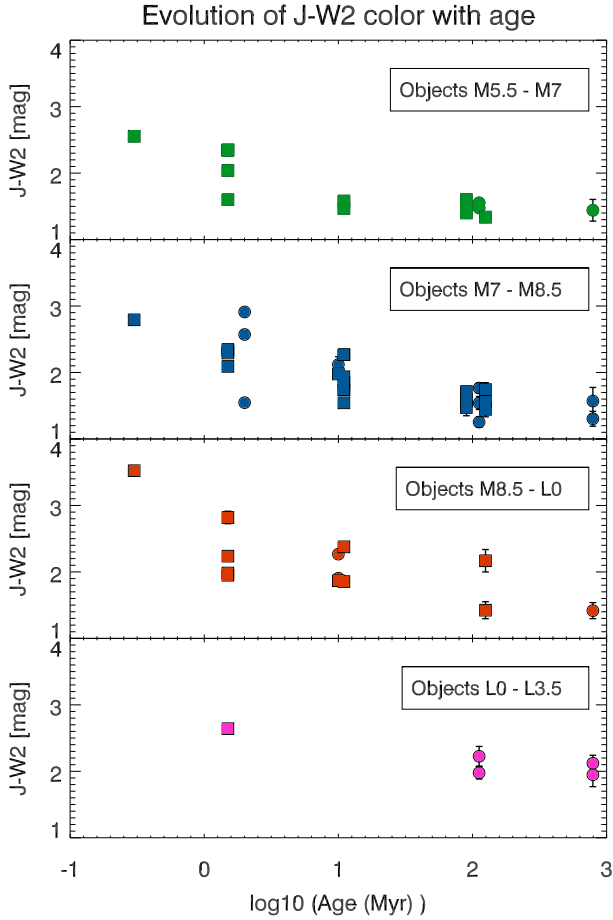


Figure 7. Log(Age) versus $J - W2$ colour for our sample (circles), and objects with well-determined ages from Martín et al. (2017), i.e. members of Alpha Persei, of UppSco, of Taurus, and from Rho Ophiuchi, separated by ranges of spectral types (squares). We observe that after the 10 Myr the $J - W2$ colour does not change significantly from the $J - W2$ colour of a field object.

$\text{erg s}^{-1}\text{cm}^{-2}\mu\text{m}^{-1}$, and d is the distance to the source in cm. We present the L_{bol} in Table 10, and we plot them vs their near-infrared spectral type in Figure 8. We overplot the polynomial fit to the spectral types versus L_{bol} plot from Filippazzo et al. (2015), obtaining similar results for the values of the L_{bol} , with exception of 2MASS J11123099-765334 from Cha I, and 2MASS J16060629-2335133 from UppSco, that are young objects. In addition, objects UGCS J083748.00+201448.5, 2MASS J08410852+1954018, 2MASS J08370450+2016033, and UGCS J084510.65+214817.0, from the Praesepe, and objects 2MASS J03484469+2437236, and 2MASS J03443516+2513429 from the Pleiades open cluster are also overluminous, as expected, given that they are binary candidates (see Table 1).

In addition, we calculated the bolometric correction for our sample using the equation:

$$BC_{\text{band}} = M_{\text{bol}} - M_{\text{band}} \quad (3)$$

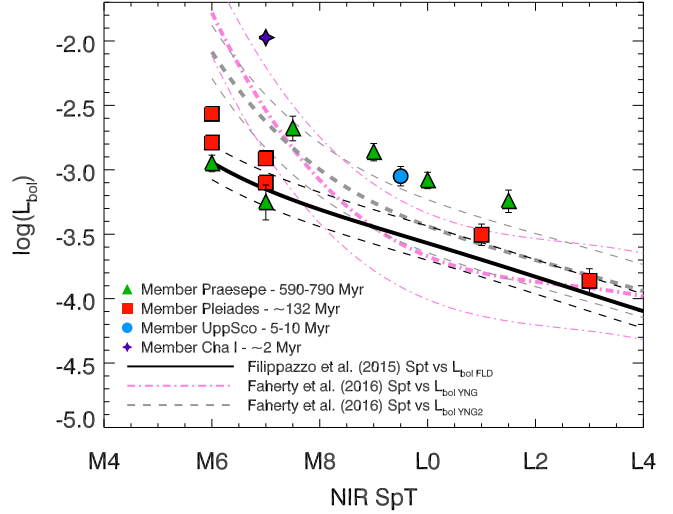


Figure 8. L_{bol} calculated for our sample following the procedure presented in Filippazzo et al. (2015). The grey solid line represents the empirical relation derived in the same work for spectral types versus L_{bol} , and the grey dashed lines delimit the rms of the empirical relation.

In Figures 9 and 10 we compare our results with the BCs obtained using the polynomial fit derived by Filippazzo et al. (2015), obtaining in general consistent between our BCs and the BCs obtained using the polynomial published in Filippazzo et al. (2015). The values obtained for the BCs for our sample are shown in Table 10. This suggests that the binary candidates, if confirmed, might have two components with similar spectral types to have BCs consistent with a single component.

5.2 Mass, Radii, effective temperature and surface gravity

We use the extension of the evolutionary models from Baraffe et al. (2015) for brown dwarfs and extrasolar planets to estimate the values of the masses, effective temperatures, radii and surface gravities for our objects with well-determined ages. In addition, we will compare the values of the surface gravities with the gravity classes defined by Allers & Liu (2013). Because not all grids for all ages are available, we use the closest one in age for the estimation of the physical parameters of our objects: for members of Cha I (~ 2 Myr), we use the grid for 2 Myr, for the members of UppSco (5–10 Myr), we use the 10 Myr grid, for the Pleiades (132 ± 27 Myr), we use the 120 Myr grid, and for members of the Praesepe (590–790 Myr), we use the 625 Myr grid. In Table 11, we show the values of the masses, effective temperatures, radii, surface gravities, gravity scores and gravity classes calculated as described in Allers & Liu (2013).

After removing binary candidates, we use evolutionary models to predict the masses for our sample (see Table 11). We estimate masses between $15.2 \pm 1.1 M_{\text{Jup}}$ and $113.6 \pm 21.4 M_{\text{Jup}}$. Most of our objects, apparently single, have masses below the hydrogen burning limit. We estimate

Table 10. Bolometric luminosity and bolometric correction for our targets in J and K -band.

Name	SpT	$Gaia$ π^a (mas)	$\log(L_{\text{bol}}/L_{\odot})$	BC_K	BC_J
UGCS J083748.00+201448.5	M6.0	3.53 ± 2.01	-2.95 ± 0.06	2.92 ± 0.16	1.77 ± 0.16
2MASS J08370215+1952074	M7.5	3.78 ± 0.80	-2.68 ± 0.09	2.99 ± 0.24	1.92 ± 0.24
UGCS J083654.60+195415.7	M7.0		-3.25 ± 0.13	2.87 ± 0.33	1.99 ± 0.33
2MASS J08410852+1954018	M9.0		-2.86 ± 0.06	2.99 ± 0.17	2.08 ± 0.17
2MASS J08370450+2016033	L0.0		-3.08 ± 0.06	3.22 ± 0.16	1.79 ± 0.16
UGCS J084510.65+214817.0	L1.5		-3.24 ± 0.09	3.28 ± 0.22	1.77 ± 0.22
2MASS J03484469+2437236	M6.0	6.81 ± 0.34	-2.57 ± 0.02	2.89 ± 0.04	1.84 ± 0.04
2MASS J03491512+2436225	M6.0	7.43 ± 0.45	-2.79 ± 0.02	2.99 ± 0.05	1.92 ± 0.05
2MASS J03512557+2345214	M7.0	4.38 ± 1.35^b	-3.09 ± 0.03	2.89 ± 0.08	1.96 ± 0.08
2MASS J03443516+2513429	M7.0	7.95 ± 0.98	-2.91 ± 0.02	3.03 ± 0.06	1.91 ± 0.06
2MASS J03463425+2350036	L1.0		-3.50 ± 0.08	3.04 ± 0.21	1.79 ± 0.21
2MASS J03461406+2321565	M7.0	7.22 ± 0.58	-2.91 ± 0.03	2.86 ± 0.08	1.92 ± 0.08
2MASS J03541027+2341402	L3.0		-3.86 ± 0.10	3.52 ± 0.23	1.81 ± 0.23
2MASS J16060629-2335133	M9.5		-3.05 ± 0.08	3.18 ± 0.19	1.80 ± 0.19
2MASS J11123099-7653342	M7.0		-1.97 ± 0.02	2.72 ± 0.05	1.93 ± 0.05

a: When the parallax for the individual object is not available, we use the average parallax to the open cluster/association to calculate the bolometric luminosity as provided in Section 2.

b: 2MASS J03512557+2345214 has a significantly different $Gaia$ parallax from the other Pleiades members, thus, it might not be a member of the Pleiades open cluster.

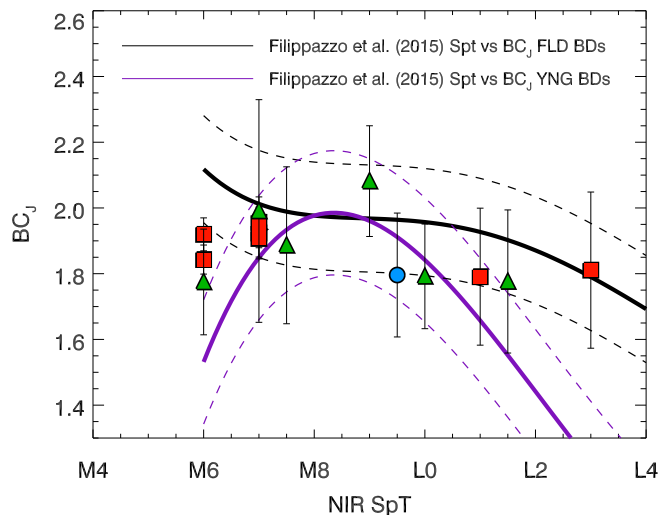


Figure 9. BC_J calculated for our sample following the procedure presented in Filippazzo et al. (2015). The black solid line represents the empirical relation derived in the same work for spectral types versus BC_J , and the black dashed lines delimit the rms of the empirical relation. The purple solid line with its respective purple dashed lines represent the same relation for young brown dwarfs.

radii between $1.11 \pm 0.14 R_{\text{Jup}}$ and $3.75 \pm 0.01 R_{\text{Jup}}$, and surface gravities between 3.51 ± 0.01 dex and 5.22 ± 0.01 dex. The Praesepe members have surface gravities higher than $\log g \sim 5.20$ dex, consistent with FLD-G gravity classification. The Pleiades members have surface gravities of $\log g \sim 4.79$ – 4.92 dex, consistent with INT-G to FLD-G classification. The UppSco members have $\log g \sim 4.07$ dex, consistent with VL-G to INT-G surface gravity classification. Finally, the Cha I member has a $\log g \sim 3.51$ dex, consistent with VL-G gravity classification.

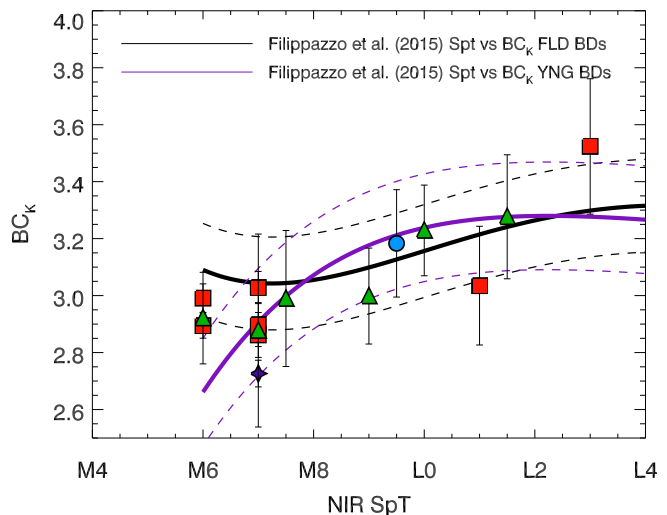


Figure 10. BC_K calculated for our sample following the procedure presented in Filippazzo et al. (2015). The black solid line represents the empirical relation derived in the same work for spectral types versus BC_K , and the black dashed lines delimit the rms of the empirical relation. The purple solid line with its respective purple dashed lines represent the same relation for young brown dwarfs.

6 CONCLUSIONS AND FINAL REMARKS

We obtained 0.6 – $2.5 \mu\text{m}$ VLT/X-shooter spectra of 20 low-mass stars and brown dwarfs members to the Cha I, (2 Myr), UppSco (5–10 Myr), Pleiades (132 ± 27 Myr) and Praesepe (590–790 Myr) open cluster. Our targets have spectral types between M6.0 and L3.0.

We performed a consistent spectral classification of our targets by comparing their optical and near-infrared spectra to both young and field M and L templates in both wavelength ranges independently. We obtained a consistent spec-

Table 11. Masses, effective temperatures, surface gravities and radii given by the evolutionary models of Baraffe et al. (2015). We exclude binary candidates and targets with reported circumstellar disks from this list.

Name	SpT	M (M_{Jup})	T_{eff} (K)	R (R_{Jup})	Log g	GC ^c	OC/A
UGCS J083748.00+201448.5	M7.0	113.6±21.4	2898±210	1.33±0.20	5.22±0.06	FLD-G	Praesepe
UGCS J083654.60+195415.7	M8.0	91.2±15.3	2590±320	1.11±0.14	5.29±0.04	INT-G	Praesepe
2MASS J03491512+2436225	M6.0	70.3±3.0	2723±33	1.46±0.03	4.92±0.01	INT-G	Pleiades
2MASS J03443516+2513429	M8.5	61.7±6.5	2621±76	1.40±0.03	4.91±0.01	FLD-G	Pleiades
2MASS J03463425+2350036	L1.0	37.0±4.5	2017±192	1.23±0.02	4.80±0.03	INT-G	Pleiades
2MASS J03461406+2321565	M6.0	56.6±4.7	2537±72	1.36±0.04	4.90±0.01	INT-G	Pleiades
2MASS J03541027+2341402	L3.0	36.2±2.3	1983±100	1.22±0.01	4.79±0.02	VL-G	Pleiades
2MASS J16060629-2335133	M9.5	15.2±1.1	2238±55	1.84±0.12	4.07±0.02	VL-G	UpSco
2MASS J11123099-7653342	M7.0	27.3±1.6	2653±21	3.75±0.01	3.51±0.14	VL-G	Cha I

c: GS: Gravity scores as described in Allers & Liu (2013). The first three gravity scores belong to the result of the pEWs of the KI lines at 1169, 1177 and 1253 nm. The rest belong to the gravity scores obtained from the spectral indices described in Section 4.2.3.

tral type for most of our objects in all the comparisons with a maximum discrepancy of ± 2.5 spectral types. The maximum dispersion in spectral type classification was reached for very young or field objects, for which the match to field or young objects respectively was more challenging to find. Finally, we adopted the spectral type obtained when comparing to near-infrared field objects as their final spectral classification.

We measured the pEWs of the alkali lines in the optical and in the near-infrared. For completion, we added other measurements for other objects with different ages (see Section 4.2.1). We found that the pEWs of the alkali lines in the optical and near-infrared increases with age, as found by previous works (Steele & Jameson 1995; Martín et al. 1996; Gorlova et al. 2003; Cushing et al. 2005; Allers & Liu 2007, and references therein). We found that members of the Pleiades have similar pEW for most of the alkali lines than field objects. The same is observed for objects of the α -Persei group (90 Myr). This fact suggests that at approximately 100 Myr, low-mass stars and brown dwarfs have nearly reached their final surface gravities, as concluded by Martín et al. (2017), and as predicted by evolutionary models for brown dwarfs (Baraffe et al. 2015).

In addition, we further investigated the relationship between pEWs of the alkali lines in the near-infrared and the age. We found a moderate correlation between the pEWs of the alkali lines in the J -band and age, for all ranges of spectral types. We observed that the increase of the pEWs with age is more remarkable for objects with spectral type later than M8. We provided relationships between pEWs and age that can be used in the future to roughly estimate ages given the pEWs of the alkali lines in the J -band.

We calculated the gravity scores defined by Allers & Liu (2007) using the alkali lines in the J -band, and the FeH_J, the KI_J, the H -cont, the FeH_Z, and the VO_Z band. We obtained a final surface gravity classification using all the indices, that reproduce reasonably well the youngest objects (Cha I and UppSco) but do not predict accurately intermediate and field M and L dwarfs. Thus, surface gravity indices must be used with caution, specially when a non low-surface gravity classification is obtained. Red colours have been believed to be a potential indicator of young age and low surface gravity (Allers & Liu 2013; Bonnefoy et al. 2014a; Manjavacas et al. 2014, and references therein). Thus, we investigated the correlation between the $J - W2$ colour and the age. We

found a moderate correlation between those two quantities for the spectral types we consider in our work. In Figures 6 and 7, we found that objects that were mostly red, have ages below ~ 10 Myr, that might be linked to the existence of a protoplanetary disk, ring structures, extinction through the star forming region, or viewing angle, but not necessarily to the influence of low surface gravity in their atmospheres. In addition, some of the members of moving groups older than 100 Myr presented in Faherty et al. (2016) show very red colours. This fact suggests that colours do not scale linearly with ages (Marocco et al. 2014; Liu et al. 2016; Bowler et al. 2017; Zapatero Osorio et al. 2017).

We calculated the bolometric luminosity of our sample using the optical, or optical Pan-STARRS photometry, near-infrared X-shooter flux calibrated spectra, and WISE photometry. We calculated the bolometric corrections in the J - and K -band, and compared them to the polynomial fits from Filippazzo et al. (2015), and Faherty et al. (2016). With exception of binary candidates, most of our targets followed the spectral type vs L_{bol} relation from Filippazzo et al. (2015). Praesepe and Pleiades non-binary candidate members followed the relation derived by Filippazzo et al. (2015) for field objects. Members of the Cha I or the UppSco association are overluminous with respect to the field and the young sequence, which is in agreement with the expectations for such young sources.

Similarly, we plot the relation between near-infrared spectral types and the BC_J, and BC_K. We overplot the spectral type vs BC_J and BC_K relation for field and young objects. All objects of our sample follow these relations, even binary candidates. This suggests that, in case our binary candidates are actually binaries, their components should have similar spectral type, so that the difference between the absolute flux in J and K bands remains similar to the difference for a single object of the same spectral type.

The surface gravities obtained for our targets using Baraffe et al. (2015) evolutionary models did not always agree with the gravity classification given by Allers & Liu (2013) indices. The gravity classification was consistent only for all objects from the Cha I and from the UppSco association. Thus, as suggested before, gravity indices should be used with caution, considering that they might not always provide an accurate spectral classification.

ACKNOWLEDGEMENTS

Based on observations collected at the European Organisation for Astronomical Research in the Southern Hemisphere under ESO programmes: 098.C-0277(A), 093.C-0109(A), and 095.C-0812(A), 093.C-0769(A), and 095.C-0378(A).

This publication makes use of data products from the Two Micron All Sky Survey, which is a joint project of the University of Massachusetts and the Infrared Processing and Analysis Center/California Institute of Technology, funded by the National Aeronautics and Space Administration and the National Science Foundation

This work is based on observations (programme GTC66-12B) made with the Gran Telescopio Canarias (GTC), operated on the island of La Palma in the Spanish Observatorio del Roque de los Muchachos of the Instituto de Astrofísica de Canarias.

This work has made use of data from the European Space Agency (ESA) mission *Gaia* (<https://www.cosmos.esa.int/gaia>), processed by the *Gaia* Data Processing and Analysis Consortium (DPAC, <https://www.cosmos.esa.int/web/gaia/dpac/consortium>). Funding for the DPAC has been provided by national institutions, in particular the institutions participating in the *Gaia* Multilateral Agreement.

N. L. and V. J. S.-B. are supported by programme AYA2015-69350-C3-2-P and MRZO by programme AYA2016-79425-C3-2-P from Spanish Ministry of Economy and Competitiveness (MINECO).

REFERENCES

- Allers K. N., Liu M. C., 2007, in American Astronomical Society Meeting Abstracts. Bulletin of the American Astronomical Society, Vol. 39, p. 103.15
- Allers K. N., Liu M. C., 2013, *ApJ*, 772, 79
- Allers K. N. et al., 2007, *ApJ*, 657, 511
- Alves de Oliveira C., Moraux E., Bouvier J., Bouy H., 2012, *A&A*, 539, A151
- Ardila D., Martín E., Basri G., 2000, *AJ*, 120, 479
- Baraffe I., Homeier D., Allard F., Chabrier G., 2015, *A&A*, 577, A42
- Barrado y Navascués D., 2004, in F. Favata, S. Aigrain, A. Wilson, eds, *Stellar Structure and Habitable Planet Finding*. ESA Special Publication, Vol. 538, pp. 269–271
- Best W. M. J. et al., 2017, *ApJ*, 837, 95
- Bihain G., Rebolo R., Zapatero Osorio M. R., Béjar V. J. S., Caballero J. A., 2010, *A&A*, 519, A93
- Bihain G., Rebolo R., Béjar V. J. S., Caballero J. A., Bailer-Jones C. A. L., Mundt R., Acosta-Pulido J. A., Manchado Torres A., 2006, *A&A*, 458, 805
- Blanton M. R. et al., 2017, *AJ*, 154, 28
- Bonnefoy M., Chauvin G., Lagrange A. M., Rojo P., Allard F., Pinte C., Dumas C., Homeier D., 2014a, *A&A*, 562, A127
- Bonnefoy M., Chauvin G., Lagrange A. M., Rojo P., Allard F., Pinte C., Dumas C., Homeier D., 2014b, *A&A*, 562, A127
- Bonnefoy M. et al., 2016, *A&A*, 587, A58
- Borysow A., Jorgensen U. G., Zheng C., 1997, *A&A*, 324, 185
- Boudreault S., Lodieu N., 2013, *MNRAS*, 434, 142
- Boudreault S., Bailer-Jones C. A. L., Goldman B., Henning T., Caballero J. A., 2010, *A&A*, 510, A27
- Boudreault S., Lodieu N., Deacon N. R., Hambly N. C., 2012, *MNRAS*, 426, 3419
- Boulanger F., Bronfman L., Dame T. M., Thaddeus P., 1998, *A&A*, 332, 273
- Bouvier J., Stauffer J. R., Martin E. L., Barrado y Navascués D., Wallace B., Bejar V. J. S., 1998, *A&A*, 336, 490
- Bouy H. et al., 2015, *A&A*, 577, A148
- Bowler B. P., Liu M. C., Shkolnik E. L., Dupuy T. J., Cieza L. A., Kraus A. L., Tamura M., 2012, *ApJ*, 753, 142
- Bowler B. P. et al., 2017, *AJ*, 153, 18
- Brandt T. D., Huang C. X., 2015, *ApJ*, 807, 24
- Breger M., 1986, *ApJ*, 309, 311
- Briceño C., Luhman K. L., Hartmann L., Stauffer J. R., Kirkpatrick J. D., 2002, *ApJ*, 580, 317
- Burgasser A. J., Geballe T. R., Leggett S. K., Kirkpatrick J. D., Golimowski D. A., 2006, *ApJ*, 637, 1067
- Burrows A. et al., 1997, *ApJ*, 491, 856
- Carpenter J. M., Mamajek E. E., Hillenbrand L. A., Meyer M. R., 2006, *ApJ*, 651, L49
- Carpenter J. M., Ricci L., Isella A., 2014, *ApJ*, 787, 42
- Cepa J., Bland-Hawthorn J., González J. J., OSIRIS Consortium, 2000, in W. van Breugel, J. Bland-Hawthorn, eds, *Imaging the Universe in Three Dimensions*. Astronomical Society of the Pacific Conference Series, Vol. 195, p. 597
- Chambers K. C. et al., 2016, arXiv e-prints
- Chauvin G., Lagrange A. M., Dumas C., Zuckerman B., Mouillet D., Song I., Beuzit J. L., Lowrance P., 2004, *A&A*, 425, L29
- Chiu K., Fan X., Leggett S. K., Golimowski D. A., Zheng W., Geballe T. R., Schneider D. P., Brinkmann J., 2006, *AJ*, 131, 2722
- Cruz K. L., Kirkpatrick J. D., Burgasser A. J., 2009, *AJ*, 137, 3345
- Cushing M. C., Rayner J. T., Vacca W. D., 2005, *ApJ*, 623, 1115
- Cushing M. C. et al., 2008, *ApJ*, 678, 1372
- Dahm S. E., 2015, *ApJ*, 813, 108
- de Zeeuw P. T., Hoogerwerf R., de Bruijne J. H. J., Brown A. G. A., Blaauw A., 1999, *AJ*, 117, 354
- Deacon N. R., Hambly N. C., 2004, *A&A*, 416, 125
- Delorme P., Collier Cameron A., Hebb L., Rostron J., Lister T. A., Norton A. J., Pollacco D., West R. G., 2011, *MNRAS*, 413, 2218
- Dupuy T. J., Liu M. C., 2012, *ApJS*, 201, 19
- Faherty J. K., Rice E. L., Cruz K. L., Mamajek E. E., Núñez A., 2013, *AJ*, 145, 2
- Faherty J. K. et al., 2016, *ApJS*, 225, 10
- Fang Q., Herczeg G. J., Rizzuto A., 2017, *ApJ*, 842, 123
- Feiden G. A., 2016, *A&A*, 593, A99
- Filippazzo J. C., Rice E. L., Faherty J., Cruz K. L., Van Gordon M. M.,Looper D. L., 2015, *ApJ*, 810, 158
- Fossati L., Bagnulo S., Landstreet J., Wade G., Kochukhov O., Monier R., Weiss W., Gebran M., 2008, *A&A*, 483, 891
- Gagné J., Lafrenière D., Doyon R., Malo L., Artigau É., 2014, *ApJ*, 783, 121
- Gaia Collaboration et al., 2018, *A&A*, 616, A1
- Gizis J. E., Allers K. N., Liu M. C., Harris H. C., Faherty J. K., Burgasser A. J., Kirkpatrick J. D., 2015, *ApJ*, 799, 203

- Gizis J. E. et al., 2012, *AJ*, 144, 94
- Golimowski D. A. et al., 2004, *AJ*, 127, 3516
- Gorlova N. L., Meyer M. R., Rieke G. H., Liebert J., 2003, *ApJ*, 593, 1074
- Gossage S., Conroy C., Dotter A., Choi J., Rosenfield P., Cargile P., Dolphin A., 2018, *ApJ*, 863, 67
- Herczeg G. J., Cruz K. L., Hillenbrand L. A., 2009, *ApJ*, 696, 1589
- Hiranaka K., Cruz K. L., Douglas S. T., Marley M. S., Baldassare V. F., 2016, *ApJ*, 830, 96
- Hodgkin S. T., Pinfield D. J., Jameson R. F., Steele I. A., Cossburn M. R., Hambly N. C., 1999, *MNRAS*, 310, 87
- Jones B. F., Stauffer J. R., 1991, *AJ*, 102, 1080
- Kirkpatrick J. D., Barman T. S., Burgasser A. J., McGovern M. R., McLean I. S., Tinney C. G., Lowrance P. J., 2006, *ApJ*, 639, 1120
- Kirkpatrick J. D. et al., 1999, *ApJ*, 519, 802
- Kirkpatrick J. D. et al., 2012, *ApJ*, 753, 156
- Knapp G. R. et al., 2004, *AJ*, 127, 3553
- Kraus A. L., Ireland M. J., Martinache F., Lloyd J. P., 2008, *ApJ*, 679, 762-782
- Lawrence A. et al., 2007, *MNRAS*, 379, 1599
- Liu M. C., Dupuy T. J., Allers K. N., 2016, *ApJ*, 833, 96
- Liu M. C. et al., 2013, *ApJ*, 777, L20
- Lodders K., 2002, *ApJ*, 577, 974
- Lodieu N., 2013, *MNRAS*, 431, 3222
- Lodieu N., Hambly N. C., Jameson R. F., Hodgkin S. T., Carraro G., Kendall T. R., 2007, *MNRAS*, 374, 372
- Lodieu N., Deacon N. R., Hambly N. C., 2012a, *MNRAS*, 422, 1495
- Lodieu N., Deacon N. R., Hambly N. C., 2012b, *MNRAS*, 422, 1495
- Lodieu N., Zapatero Osorio M. R., Béjar V. J. S., Pena Ramirez K., 2017, *ArXiv e-prints*
- Lodieu N., Zapatero Osorio M. R., Béjar V. J. S., Peña Ramirez K., 2018, *MNRAS*, 473, 2020
- Lodieu N., Pérez-Garrido A., Smart R. L., Silvotti R., 2019, *A&A*, 628, A66
- Long F. et al., 2017, *ApJ*, 844, 99
- López Martí B., Eisloffel J., Scholz A., Mundt R., 2004, *A&A*, 416, 555
- Luhman K. L., 2004, *ApJ*, 602, 816
- Luhman K. L., 2007, *ApJS*, 173, 104
- Luhman K. L., Mamajek E. E., 2010, *ApJ*, 716, L120
- Luhman K. L., Muench A. A., 2008, *ApJ*, 684, 654-662
- Luhman K. L., Herrmann K. A., Mamajek E. E., Esplin T. L., Pecaú M. J., 2018, *AJ*, 156, 76
- Malo L., Doyon R., Lafrenière D., Artigau É., Gagné J., Baron F., Riedel A., 2013, *ApJ*, 762, 88
- Mamajek E. E., 2005, *ApJ*, 634, 1385
- Mamajek E. E., Lawson W. A., Feigelson E. D., 2000, *ApJ*, 544, 356
- Manara C. F. et al., 2017, *A&A*, 604, A127
- Manjavacas E. et al., 2014, *A&A*, 564, A55
- Marocco F. et al., 2014, *MNRAS*, 439, 372
- Marois C., Macintosh B., Barman T., Zuckerman B., Song I., Patience J., Lafrenière D., Doyon R., 2008, *Science*, 322, 1348
- Martín E. C. et al., 2017, *ApJ*, 838, 73
- Martín E. L., Rebolo R., Zapatero-Osorio M. R., 1996, *ApJ*, 469, 706
- Martín E. L., Delfosse X., Guieu S., 2004, *AJ*, 127, 449
- Martín E. L., Lodieu N., Pavlenko Y., Béjar V. J. S., 2018, *ApJ*, 856, 40
- McGovern M. R., Kirkpatrick J. D., McLean I. S., Burgasser A. J., Prato L., Lowrance P. J., 2004, *ApJ*, 600, 1020
- McLean I. S., McGovern M. R., Burgasser A. J., Kirkpatrick J. D., Prato L., Kim S. S., 2003, *ApJ*, 596, 561
- Moraux E., Bouvier J., Stauffer J. R., Cuillandre J. C., 2003, *A&A*, 400, 891
- Nagashima C. et al., 2003, *MNRAS*, 343, 1263
- Netopil M., Paunzen E., Heiter U., Soubiran C., 2016, *A&A*, 585, A150
- Pecaú M. J., Mamajek E. E., 2016, *MNRAS*, 461, 794
- Pecaú M. J., Mamajek E. E., Bubar E. J., 2012, *ApJ*, 746, 154
- Persi P. et al., 2000, *A&A*, 357, 219
- Pinfield D. J., Dobbie P. D., Jameson R. F., Steele I. A., Jones H. R. A., Katsiyannis A. C., 2003, *MNRAS*, 342, 1241
- Prusti T., Clark F. O., Whittet D. C. B., Laureijs R. J., Zhang C. Y., 1991, *MNRAS*, 251, 303
- Rizzuto A. C., Ireland M. J., Dupuy T. J., Kraus A. L., 2016, *ApJ*, 817, 164
- Roccatagliata V., Sacco G. G., Franciosi E., Randich S., 2018, *ArXiv e-prints*
- Schlieder J. E., Lépine S., Rice E., Simon M., Fielding D., Tomasino R., 2012, *AJ*, 143, 114
- Schneider A. C., Windsor J., Cushing M. C., Kirkpatrick J. D., Shkolnik E. L., 2017, *AJ*, 153, 196
- Schneider A. C., Cushing M. C., Kirkpatrick J. D., Mace G. N., Gelino C. R., Faherty J. K., Fajardo-Acosta S., Sheppard S. S., 2014, *AJ*, 147, 34
- Skrutskie M. F. et al., 2006, *AJ*, 131, 1163
- Slesnick C. L., Hillenbrand L. A., Carpenter J. M., 2008, *ApJ*, 688, 377
- Soderblom D. R., Laskar T., Valenti J. A., Stauffer J. R., Rebull L. M., 2009, *AJ*, 138, 1292
- Song I., Zuckerman B., Bessell M. S., 2012, *AJ*, 144, 8
- Spina L. et al., 2014, *A&A*, 568, A2
- Stauffer J. R., Hartmann L. W., 1986, *ApJS*, 61, 531
- Stauffer J. R., Schultz G., Kirkpatrick J. D., 1998, *ApJ*, 499, L199
- Stauffer J. R. et al., 1999, *ApJ*, 527, 219
- Steele I. A., Jameson R. F., 1995, *MNRAS*, 272, 630
- Stephens D. C. et al., 2009, *ApJ*, 702, 154
- Taylor B. J., 2006, *AJ*, 132, 2453
- Theodossiou E., Danezis E., 1991, *Ap&SS*, 183, 91
- Tody D., 1986, in D.L. Crawford, ed., *Instrumentation in astronomy VI. Proc. SPIE, Vol. 627*, p. 733
- Tody D., 1993, in R.J. Hanisch, R.J.V. Brissenden, J. Barnes, eds, *Astronomical Data Analysis Software and Systems II. Astronomical Society of the Pacific Conference Series, Vol. 52*, p. 173
- van der Plas G. et al., 2016, *ApJ*, 819, 102
- Vernet J. et al., 2011, *A&A*, 536, A105
- Vos J. M., Allers K. N., Biller B. A., 2017, *ApJ*, 842, 78
- West A. A. et al., 2011, *AJ*, 141, 97
- Wilking B. A., Meyer M. R., Robinson J. G., Greene T. P., 2005, *AJ*, 130, 1733
- Winston E. et al., 2012, *A&A*, 545, A145
- Zakhochay O. V., Zapatero Osorio M. R., Béjar V. J. S., Boehler Y., 2017, *MNRAS*, 464, 1108

- Zapatero Osorio M. R., Rebolo R., Martín E. L., 1997,
A&A, 317, 164
Zapatero Osorio M. R., Béjar V. J. S., Peña Ramírez K.,
2017, ApJ, 842, 65

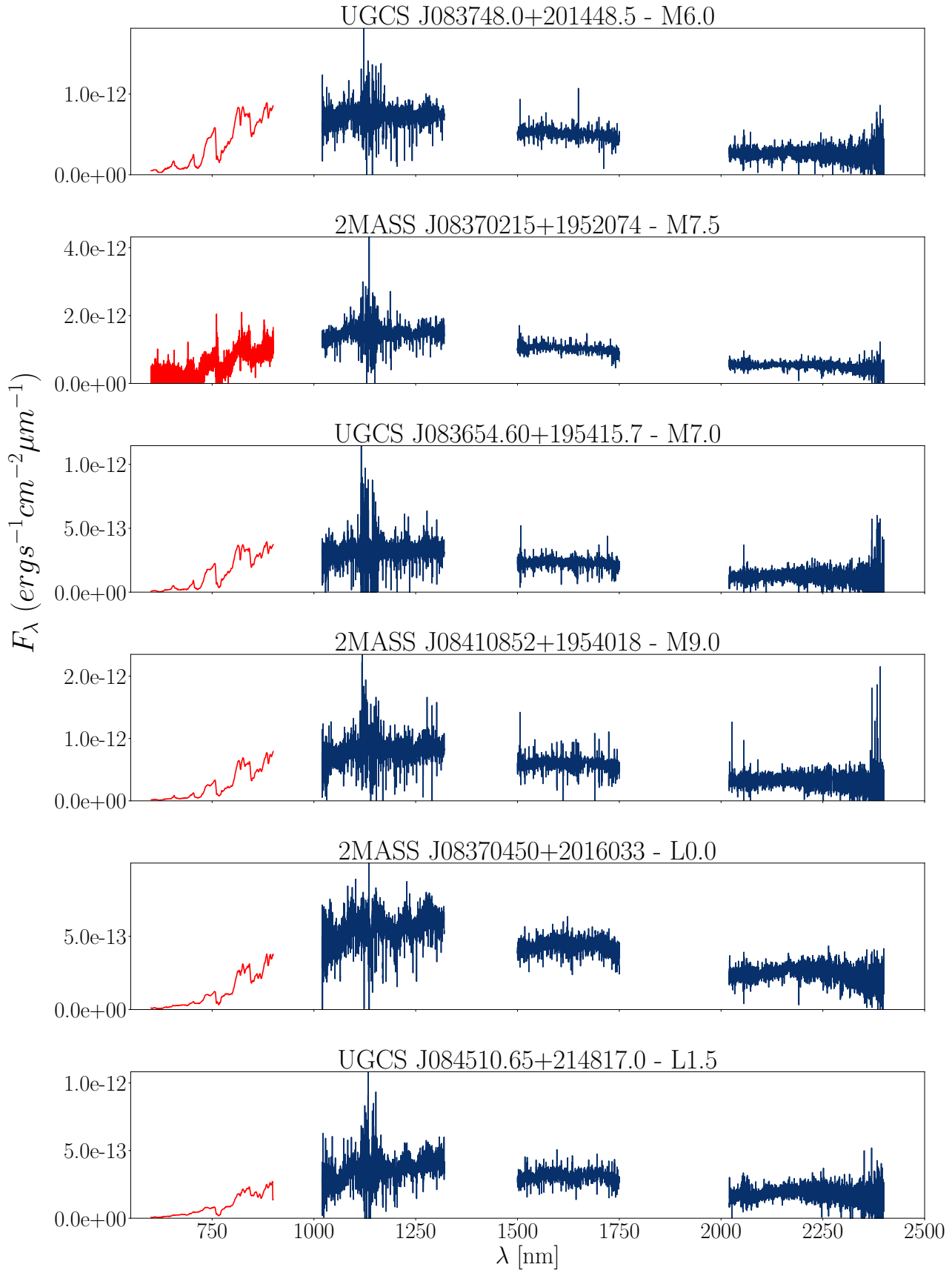


Figure 1. X-shooter/VLT and OSIRIS/GTC spectra for objects members from the Praesepe open cluster listed in Table 1. The OSIRIS or X-shooter optical spectra is shown in red for clarity. The flux density is given in F_λ in $\text{erg s}^{-1} \text{cm}^{-2} \mu\text{m}^{-1}$.

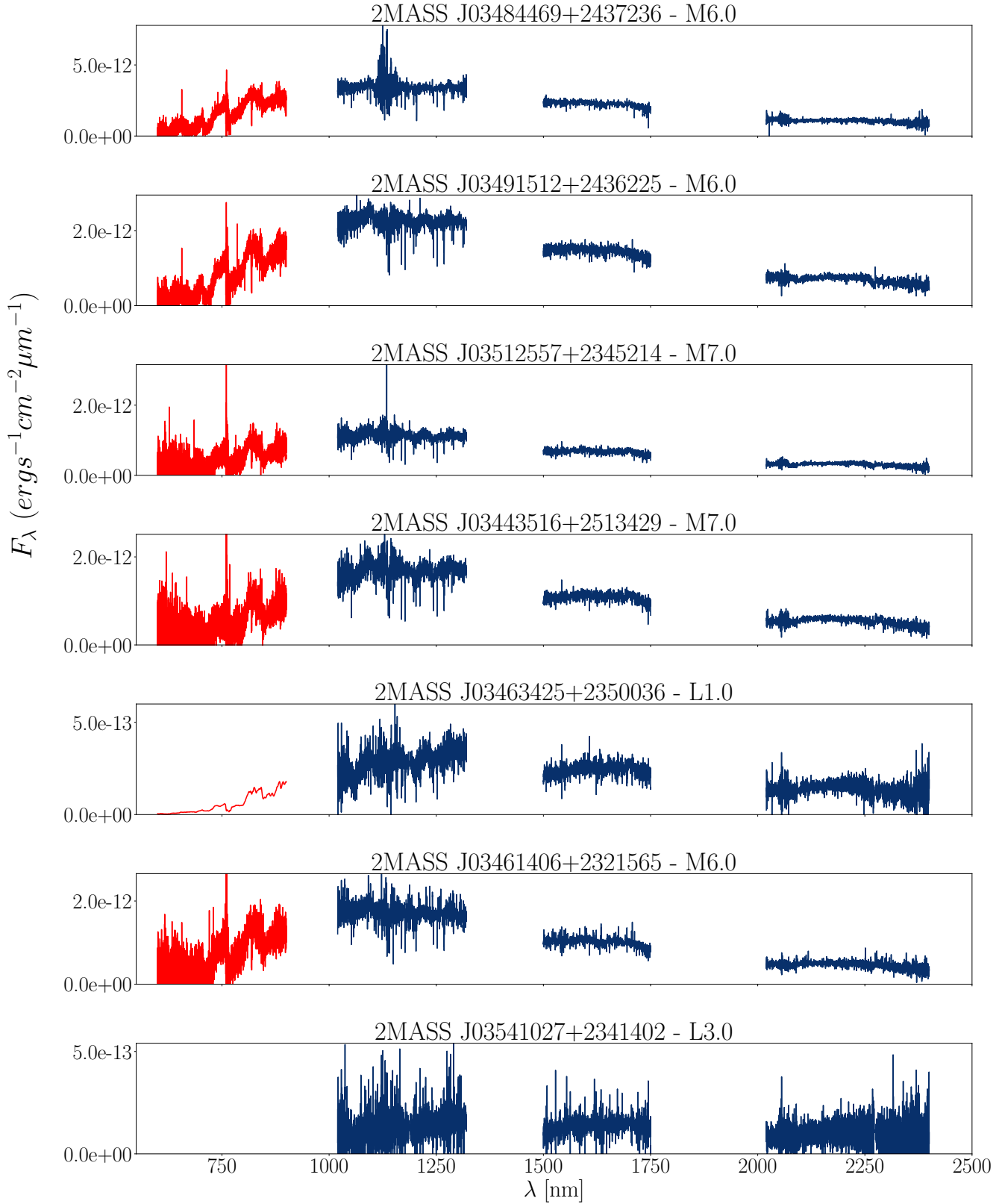


Figure 2. X-shooter/VLT and OSIRIS/GTC spectra for objects members from the Pleiades open cluster listed in Table 1. The X-shooter optical spectra is shown in red for clarity. The flux density is given in F_λ in $\text{erg s}^{-1} \text{cm}^{-2} \mu\text{m}^{-1}$.

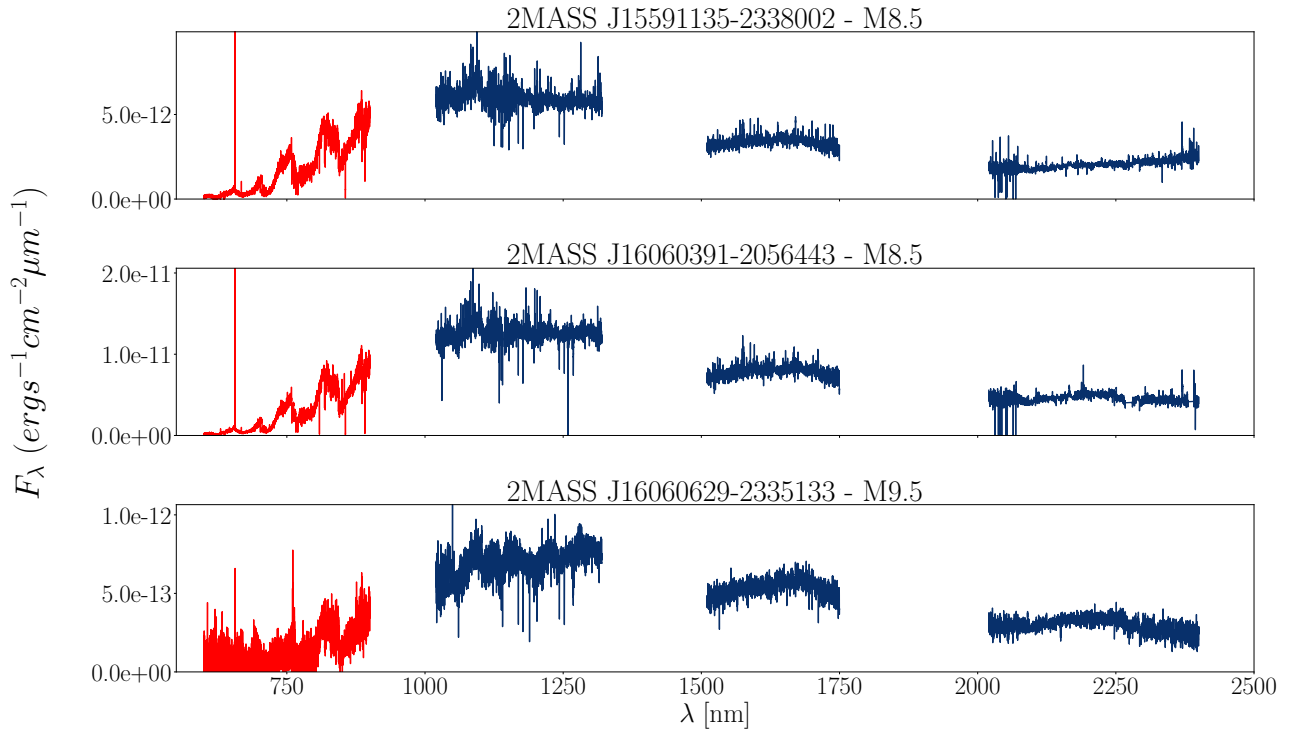


Figure 3. X-shooter/VLT and OSIRIS/GTC spectra for objects members from the UppSco association listed in Table 1. The X-shooter optical spectra is shown in red for clarity. The flux density is given in F_{λ} in $\text{erg s}^{-1} \text{cm}^{-2} \mu\text{m}^{-1}$.

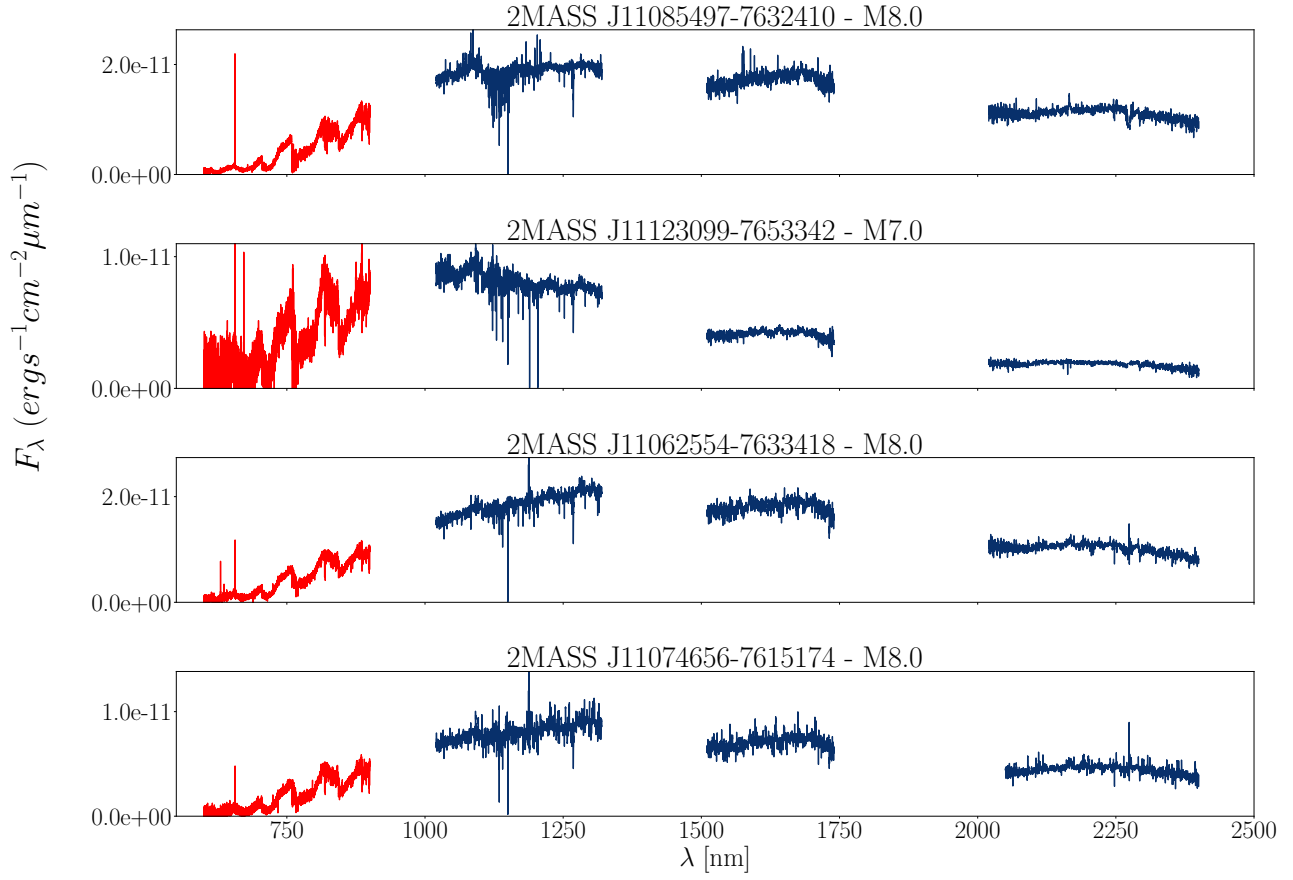


Figure 4. X-shooter/VLT and OSIRIS/GTC spectra for objects members from the Cha I association listed in Table 1. The X-shooter optical spectra is shown in red for clarity. The flux density is given in F_λ in $\text{erg s}^{-1}\text{cm}^{-2}\mu\text{m}^{-1}$.

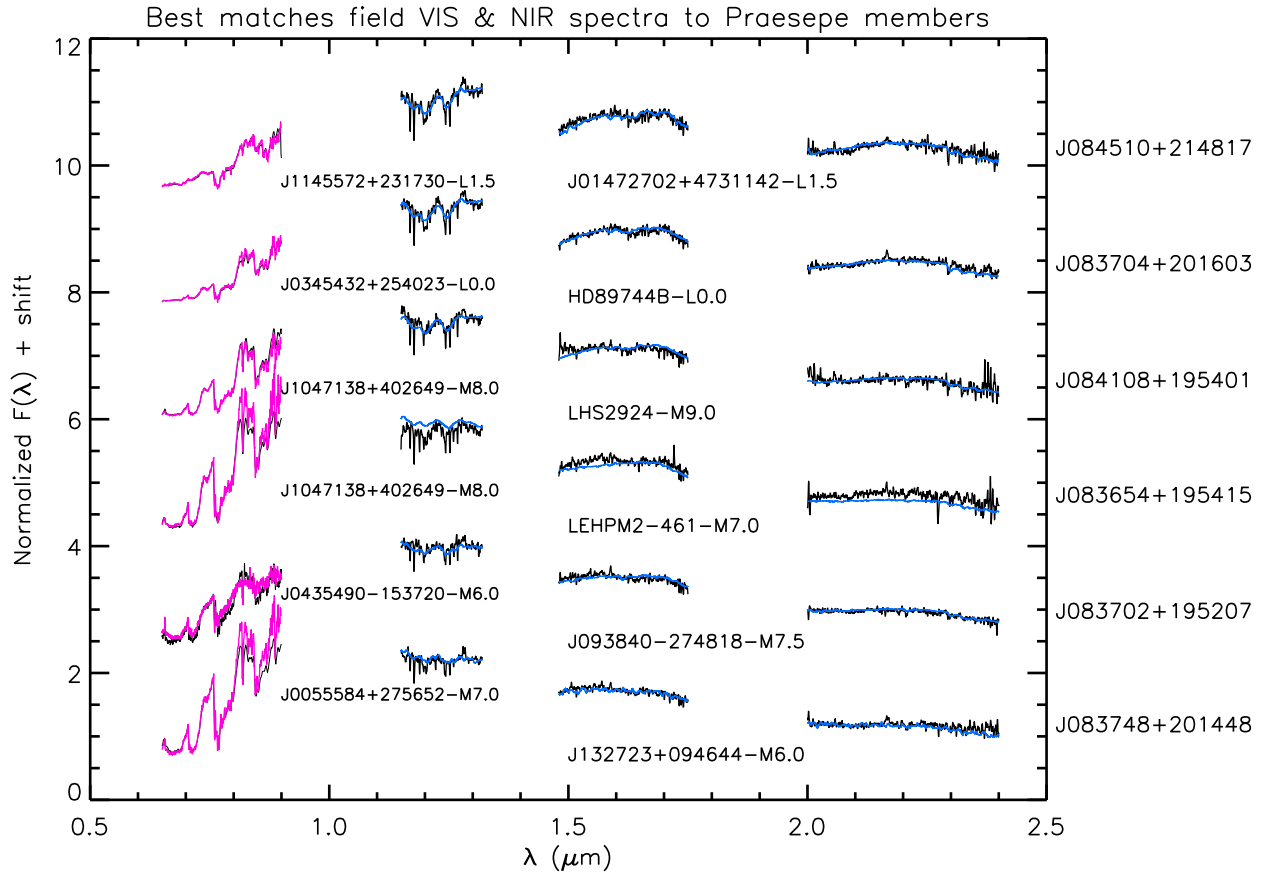
Table 1. Log of the observed targets with VLT/Xshooter.

Name	Date	Arm	DIT (s)	NINT	Seeing (")	SNR VIS/NIR	Airmass	Notes
UGCS J083748.00+201448.5	Jan 29, 2017	VIS/NIR	305/300	4/4	0.73	1.9/7.2	1.49	
Hip040881	Jan 29, 2017	VIS/NIR.	6.25/30	2/2	0.94		1.55	B9.5V Telluric Standard
2MASS J08370215+1952074	Jan 28, 2017	VIS/NIR	305/300	10/7	0.9	3.5/12.1	1.58	
Hip040881	Jan 28, 2017	VIS/NIR	5/10	2/2	0.66		1.62	B9.5V Telluric Standard
UGCS J083654.60+195415.7	Jan 23, 2017	VIS/NIR	305/300	10/7	0.83	0.9/4.5	1.51	
Hip043564	Jan 23, 2017	VIS/NIR	40/90	2/2	0.8		1.50	B5V Telluric Standard
J08410852+1954018	Jan 23, 2017	VIS/NIR	305/300	8/8	1.02	1.2/7.9	1.41	
Hip043564	Jan 23, 2017	VIS/NIR	40/90	2/2	0.92		1.5	B5V Telluric Standard
2MASS J08370450+2016033	Jan 1, 2017	VIS/NIR	305/300	8/8	0.51	1.0/8.2	1.50	
Hip022597	Jan 1, 2017	VIS/NIR	12.5/30	1/1	1.1		1.05	B5V Telluric Standard
UGCS J084510.65+214817.0	Jan 2, 2017	VIS/NIR	305/300	10/10	0.6	0.6/5.0	1.46	
Hip026545	Jan 2, 2017	VIS/NIR	12.5/30	2/2	0.74		1.49	B6V Telluric Standard
2MASS J03484469+2437236	Nov 30, 2016	VIS/NIR	305/300	6/6	0.67	9.0/24.6	1.53	
Hip009534	Jan 4, 2010	VIS/NIR	6/5	1/1	1.1		1.1	B6V Telluric Standard
2MASS J03491512+2436225	Nov 27, 2016	VIS/NIR	305/300	6/6	0.34	6.7/23.2	1.61	
Hip017900	Nov 27, 2016	VIS/NIR	6/10	2/2	0.6		1.51	B8V Telluric Standard
2MASS J03512557+2345214	Nov 26, 2016	VIS/NIR	305/300	8/8	0.4	2.8/13.4	1.51	
Hip021013	Nov 26, 2016	VIS/NIR	8/10	2/2	0.45		1.51	B8III Telluric Standard
2MASS J03443516+2513429	Nov 20, 2016	VIS/NIR	305/300	6/6	1.22	2.8/18.9	1.82	
Hip022527	Nov 20, 2016	VIS/NIR	12.5/30	2/2	1.0		1.72	B3V Telluric Standard
2MASS J03463425+2350036	Nov 11, 2016	VIS/NIR	305/300	10/10	0.28	0.5/5.2	1.58	
Hip020789	Nov 11, 2016	VIS/NIR	6/7	2/2	0.27		1.65	B7V Telluric Standard
2MASS J03461406+2321565	Nov 3, 2016	VIS/NIR	305/300	6/14	0.84	4.1/15.4	2.09	
Hip054006	Nov 3, 2016	VIS/NIR	15/23	2/2	0.9		1.91	B5V Telluric Standard
2MASS J03541027+2341402	Nov 3, 2016	VIS/NIR	305/300	14/14	1.04	0.1/3.6	1.68	
Hip045125	Nov 3, 2016	VIS/NIR	15/12	2/2	0.77		1.52	B9V Telluric Standard
2MASS J15591135-2338002	Apr 25, 2014	VIS/NIR	866/227.5	3/3	1.64	25.2/21.6	1.09	
Hip079073	Apr 25, 2014	VIS/NIR	20/20	2/2	1.50		1.09	G2V Telluric Standard
2MASS J16060391-2056443	Apr 08, 2014	VIS/NIR	866/27.5	3/3	1.47	38.8/45.7	1.00	
Hip074389	Apr 08, 2014	VIS/NIR	6.5/8	2/2	1.01		1.01	G1.5V Telluric Standard
2MASS J16060629-2335133	Jun 25, 2014	VIS/NIR	197/190	14/14	0.99	2.2/13.8	1.21	
Hip087314	Jun 25, 2014	VIS/NIR	6.25/30	2/2	1.00		1.62	B2/3Vnn Telluric Standard
2MASS J11085497-7632410	May 5, 2015	VIS/NIR	645/245	4/4	1.03	13.0/21.1	1.69	
Hip061066	May 5, 2015	VIS/NIR	25/20	2/2	1.17		1.58	B9V Telluric Standard
2MASS J11123099-7653342	Jan 14, 2017	VIS/NIR	305/300	6/6	0.8	11.5/53.6	1.63	
Hip053024	Jan 14, 2017	VIS/NIR	9/20	2/2	0.75		1.65	B4V Telluric Standard
2MASS J11074656-7615174	Apr 3, 2015	VIS/NIR	585/225	4/4	1.4	30.2/16.4	1.67	
Hip061066	Apr 3, 2015	VIS/NIR	12.5/15	2/2	0.83		1.59	B9V Telluric Standard
Cha J11070768-7626326	Apr 5, 2015	VIS/NIR	585/225	4/4	1.35	17.7/39.4	1.65	
Hip061066	Apr 5, 2015	VIS/NIR	15/20	2/2	1.63		1.58	B9V Telluric Standard

This paper has been typeset from a \TeX / \LaTeX file prepared by the author.

Table 2. Observing log for objects observed with GTC/OSIRIS: .

Name	Resolution	Num. exp. \times exp. time (s)	Observing date
UGCS J083748.00+201448.5	R300R	1 \times 900 s	17 Dec 2012
2MASS J08410852+1954018	R300R	1 \times 900 s	15 Dec 2012
UGCS J083654.60+195415.7	R300R	3 \times 600 s	03 Feb 2013
2MASS J08370215+1952074	R300R	1 \times 900 s	20 Jan 2013
UGCS J084510.65+214817.0	R300R	6 \times 700 s	16 Jan 2013
2MASS J08370450+2016033	R300R	3 \times 700 s	16 Jan 2013
2MASS J03463425+2350036	R300R	3 \times 700 s	17 Jan 2013

**Figure 5.** Best field dwarf matches (coloured lines) in the optical and near-infrared for Praesepe members (black).

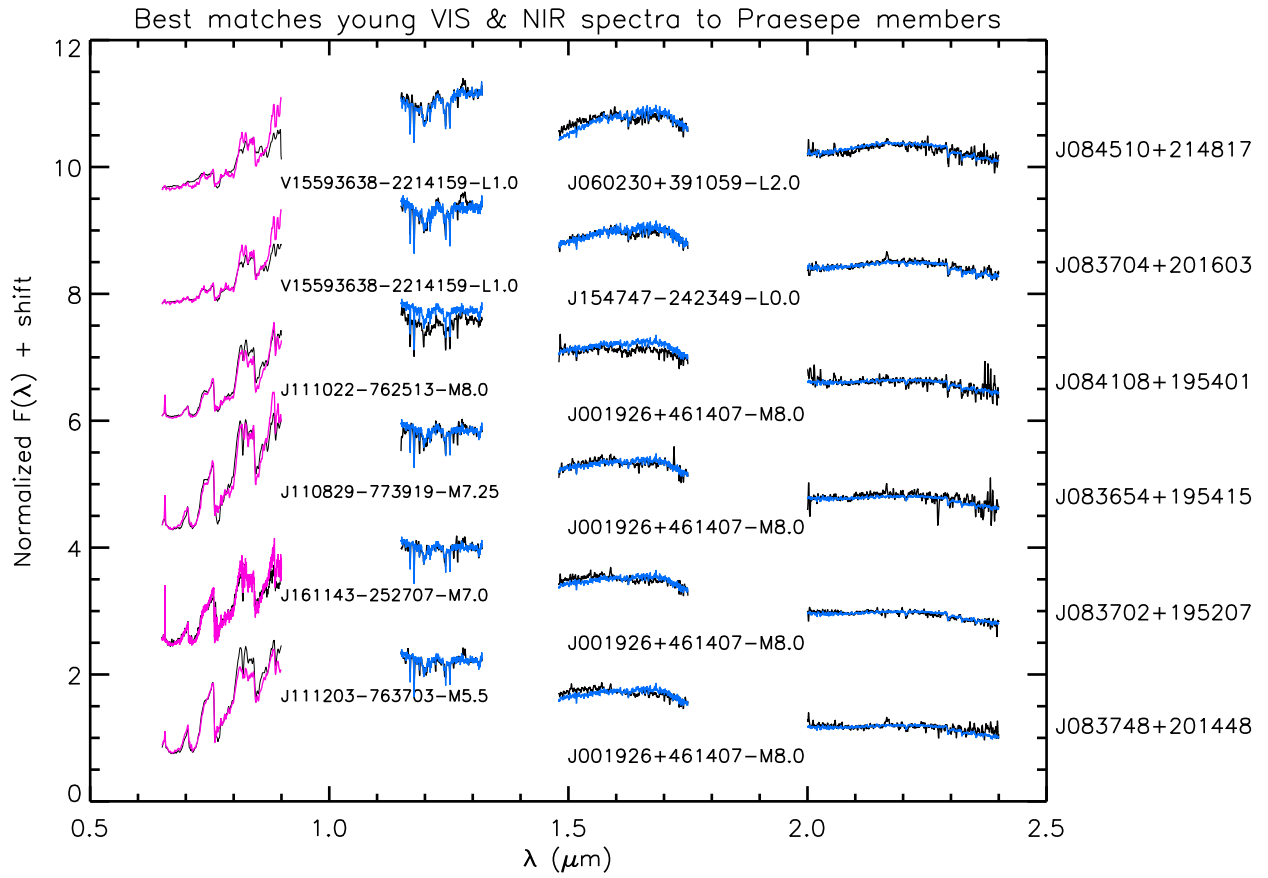


Figure 6. Same as Figure 5 but comparing with the library of young M and L dwarfs.

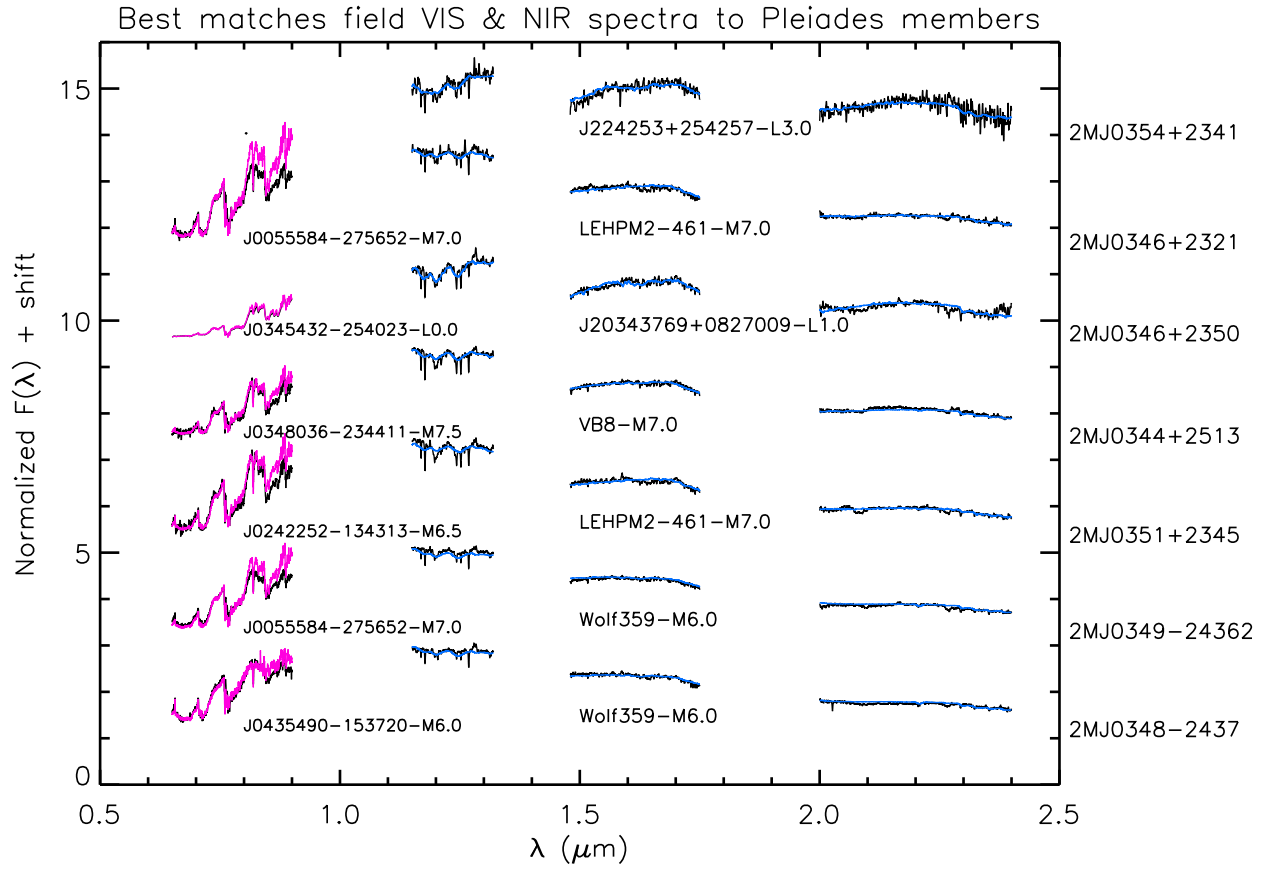


Figure 7. Best field dwarf matches (coloured lines) in the optical and near-infrared for Pleiades members (black).

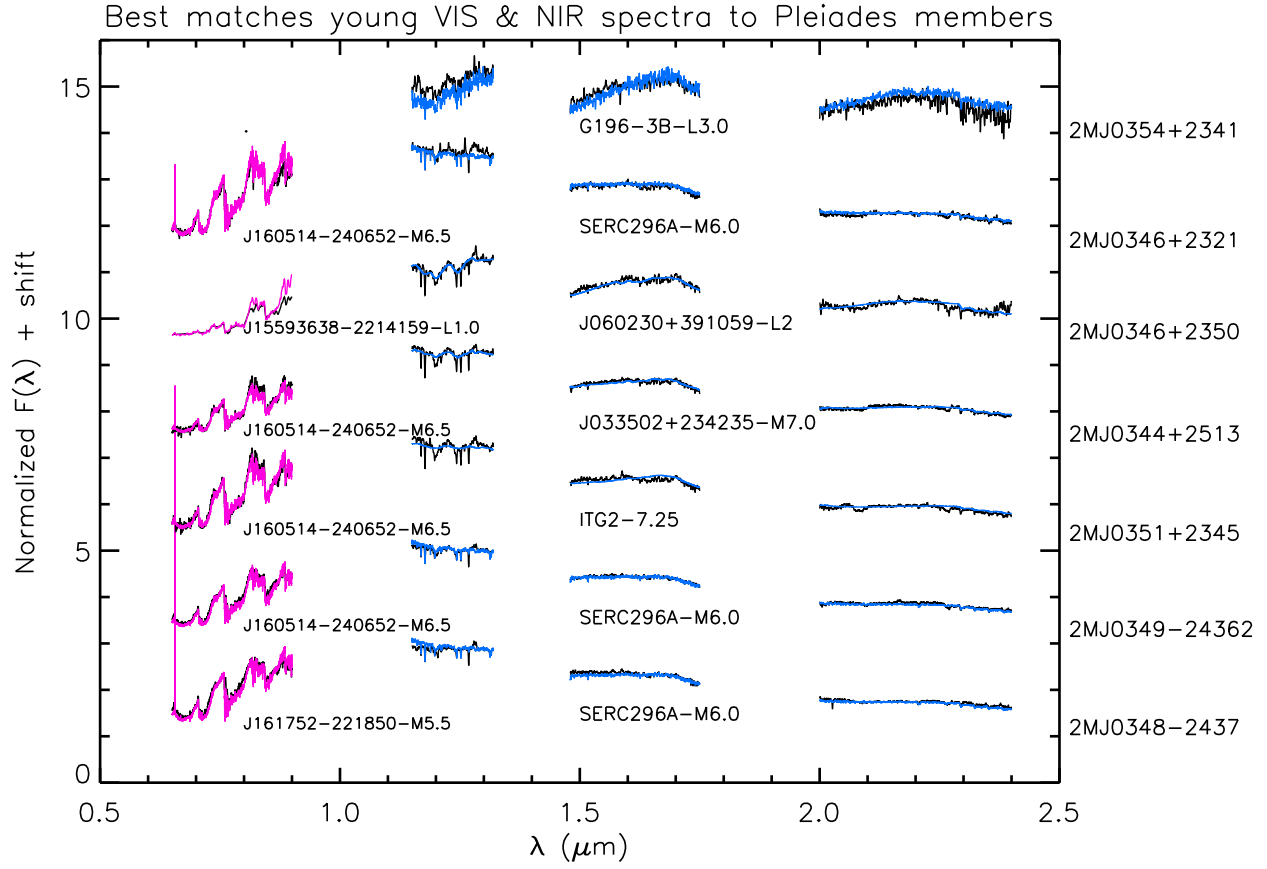


Figure 8. Same as Figure 7 but comparing with the library of young M and L dwarfs.

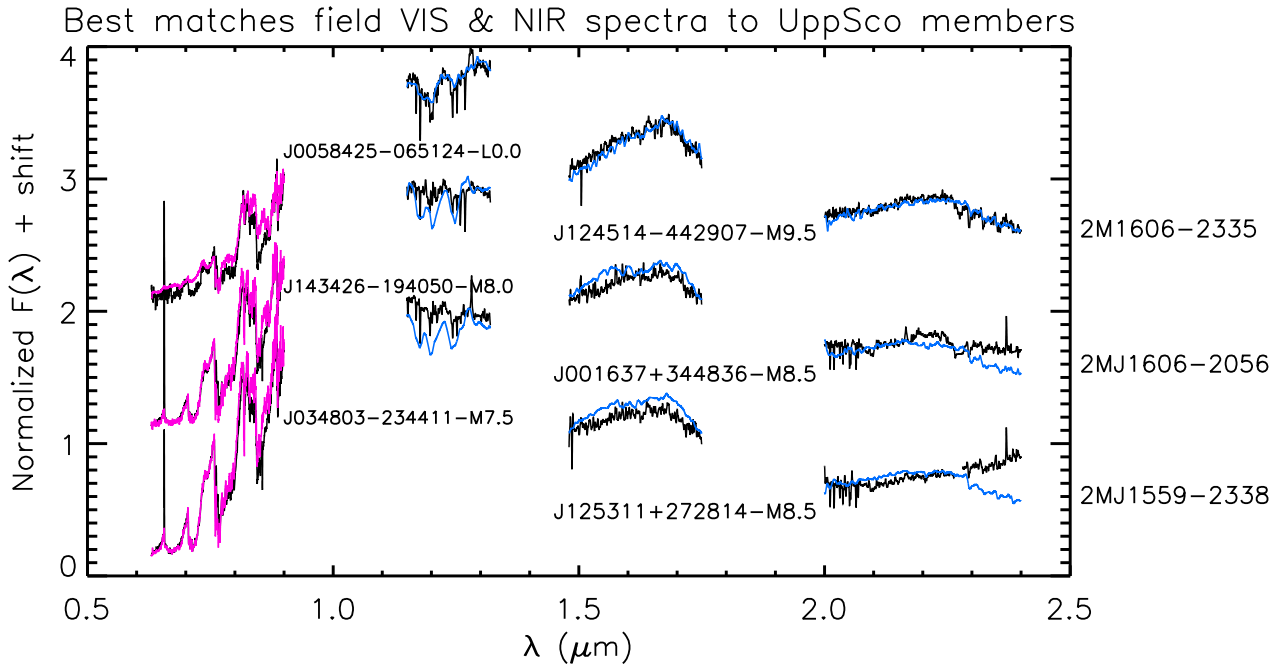


Figure 9. Best field dwarf matches (coloured lines) in the optical and near-infrared for UppSco members (black).

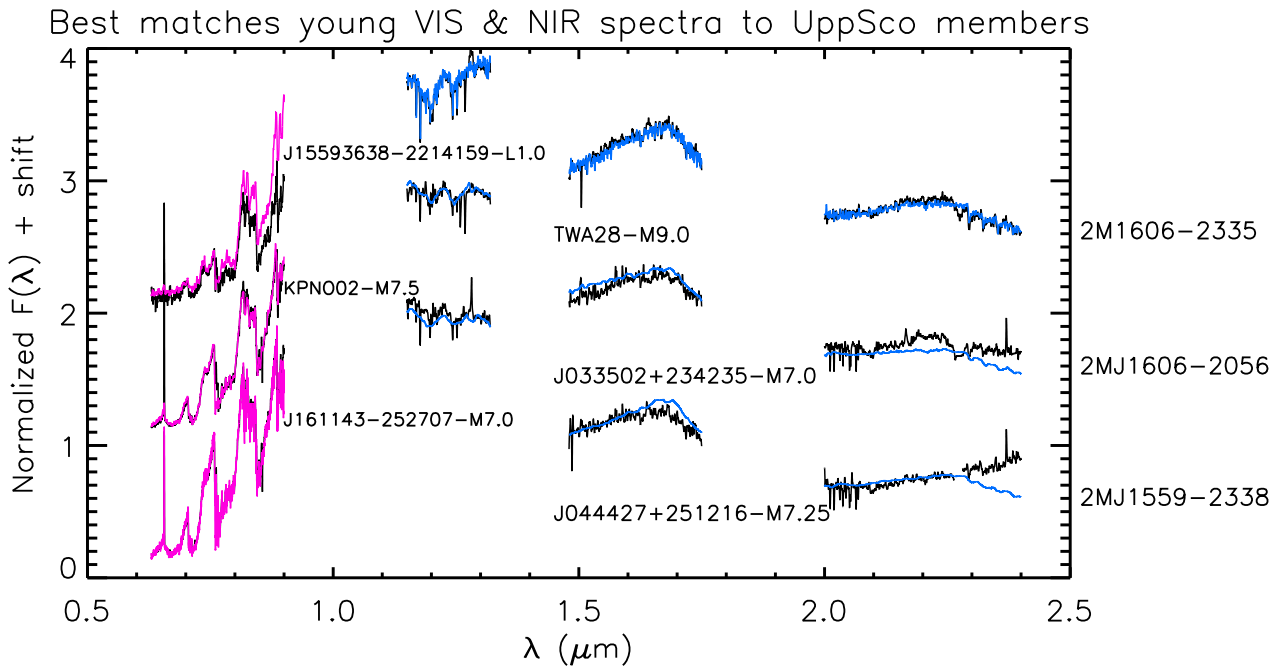


Figure 10. Same as Figure 9 but comparing with the library of young M and L dwarfs.

Best matches field VIS & NIR spectra Chamaeleon members

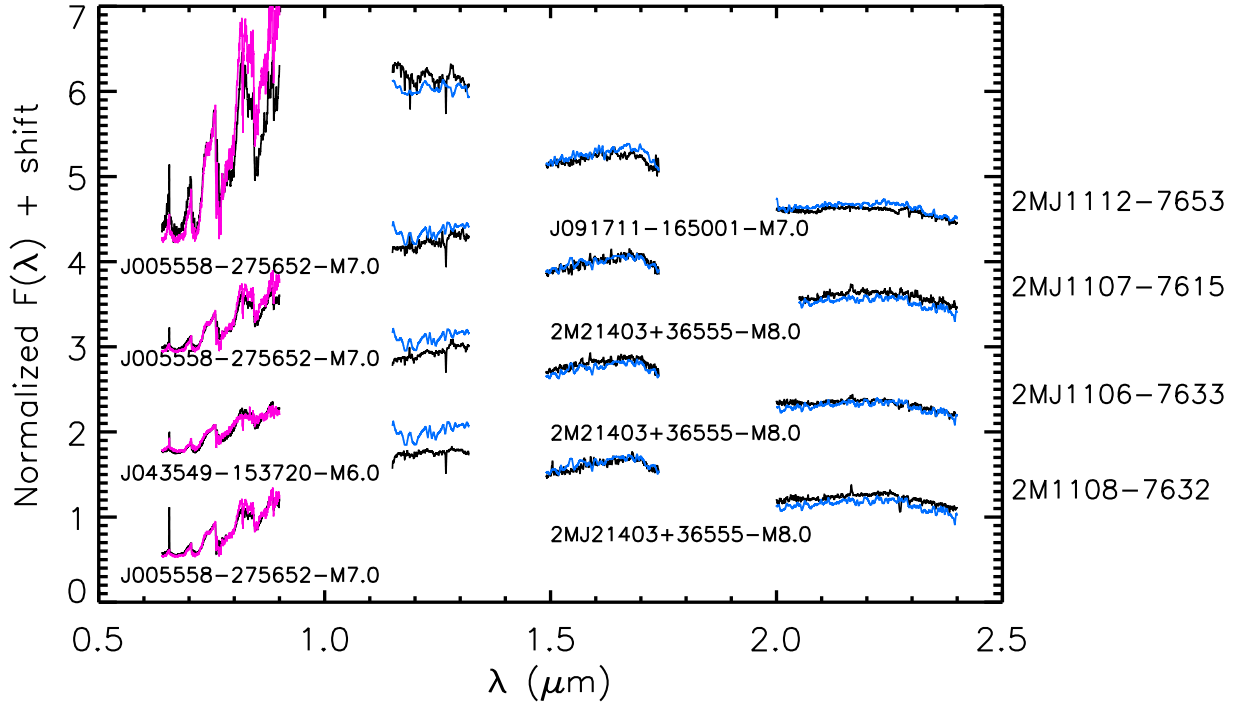


Figure 11. Best field dwarf matches (coloured lines) in the optical and near-infrared for Cha I members (black).

Best matches young VIS & NIR spectra Chamaeleon members

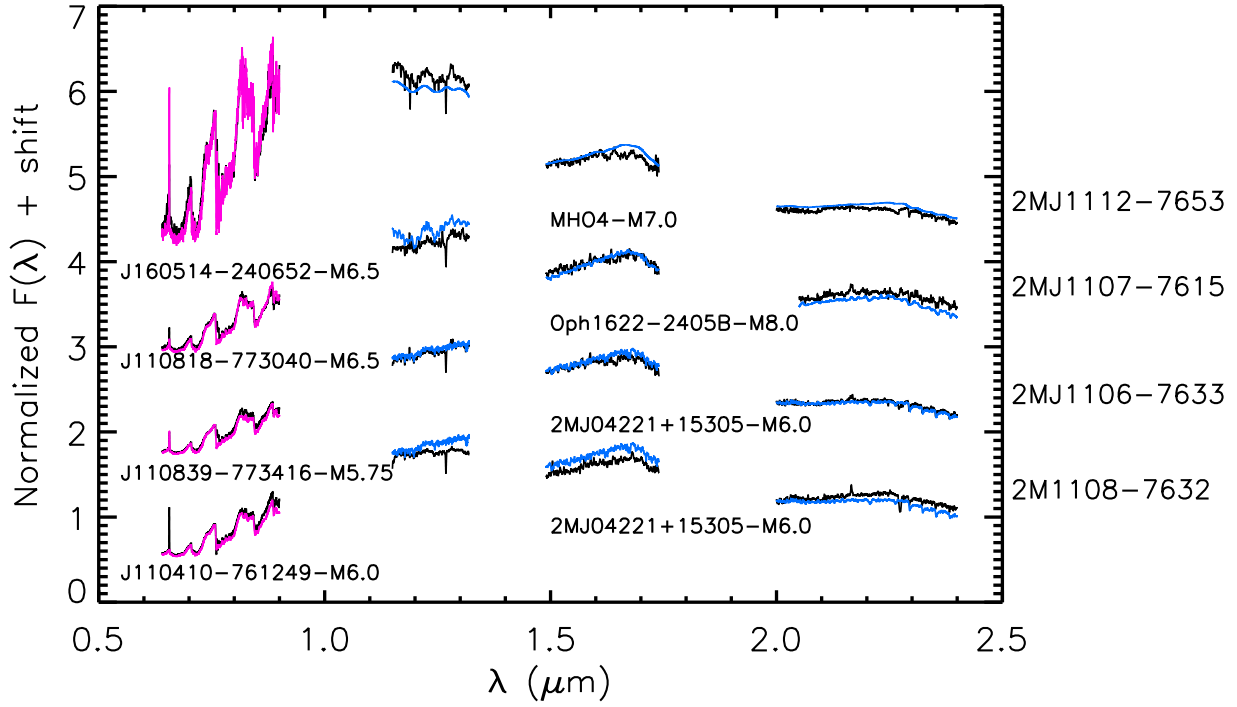


Figure 12. Same as Figure 11 but comparing with the library of young M and L dwarfs.